THESIS FOR THE DEGREE OF LICENTIATE OF ENGINEERING

Direct H_2O_2 synthesis over dilute PdAu alloys

Rasmus Svensson

Department of Physics
CHALMERS UNIVERSITY OF TECHNOLOGY
Göteborg, Sweden 2024

Direct H_2O_2 synthesis over dilute PdAu alloys
Rasmus Svensson

Department of Physics
Chalmers University of Technology
se-412 96 Göteborg, Sweden
Telephone +46 (0)31 772 10 00

Cover: Visualization of different reactions over a dilute PdAu nanoparticle.

Printed at Chalmers digitaltryck
Göteborg, Sweden 2024

Direct H_2O_2 synthesis over dilute PdAu alloys

Rasmus Svensson
Department of Physics
Chalmers University of Technology

Abstract

Heterogeneous catalysis is crucial in a range of technological and industrial processes. Depending on the composition of the catalyst and the reaction conditions, it is possible to steer the activity and the selectivity towards the desired products. However, finding a proper catalyst for a specific reaction is difficult, and several reactions still lack efficient catalysts. To aid the search for new catalysts, atomic scale understanding is desirable. In this thesis, kinetic Monte Carlo simulations are used for atomistic simulations of reaction kinetics.

The direct formation of H_2O_2 from H_2 and O_2 over single atom alloy (Pd@Au) nanoparticles, in an aqueous solution, is investigated and compared to the reaction on extended surfaces. The influence of the metal-water interface is studied using *ab initio* molecular dynamics simulations. To investigate the durability of the dilute alloy particles, kinetic Monte Carlo simulations are employed to simulate the activation and deactivation of the catalyst.

Pd monomers are found to act as active centers for H_2 dissociation, whereas the formation of H_2O_2 occurs on Au atoms located at the edges and corners of the nanoparticle. The kinetic coupling between Pd and Au sites is crucial to maintain a high selectivity towards H_2O_2. Hydrogen adsorbed on the surface is found to undergo a charge separation, where a proton desorbs to the water solution, whereas the electron is trapped in the metal. The simulations reveal that the process is facile at room temperature over a range of metal (111) surfaces, thus, providing reaction pathways that drastically differ from conventional surface reactions. Kinetic Monte Carlo simulations show that the dilute alloy particles are deactivated at elevated temperatures, in the absence of adsorbates. The deactivation depends both on the positions of the Pd monomers, and the global structure of the system.

Keywords: catalysis, kinetic modeling, kinetic Monte Carlo, density functional theory, metal-water interface, dynamics, H_2O_2 synthesis, dilute alloys

LIST OF APPENDED PAPERS

This thesis is based on work presented in the following papers:

I **Site Communication in Direct Formation of H_2O_2 over Single-Atom Pd@Au Nanoparticles**
Rasmus Svensson and Henrik Grönbeck
J. Am. Chem. Soc., 145, 21, 11579–11588, 2023

II **Spontaneous Charge Separation at the Metal-Water Interface**
Rasmus Svensson and Henrik Grönbeck
ChemPhysChem, In press

III **Dynamics of Dilute Nanoalloy Activation and Deactivation**
Rasmus Svensson and Henrik Grönbeck
In manuscript

My contribution to the papers included in the thesis:

I I performed all calculations, implemented the kinetic Monte Carlo simulations and wrote the first draft of the paper. The paper was finalised together with my co-author.

II I performed all calculations and wrote the first draft of the paper. The paper was finalised together with my co-author.

III I performed all calculations, implemented the kinetic Monte Carlo simulations and wrote the first draft of the manuscript. The manuscript was finalised together with my co-author.

Contents

1 Introduction **1**
- 1.1 Heterogeneous Catalysis . . . 2
- 1.2 Computational Approaches in Catalysis . . . 3
- 1.3 Direct H_2O_2 synthesis from H_2 and O_2 . . . 5
- 1.4 Objectives . . . 5

2 The Potential Energy Surface **7**
- 2.1 The Schrödinger Equation . . . 9
  - 2.1.1 The Born-Oppenheimer Approximation . . . 9
  - 2.1.2 The Electronic Density . . . 10
  - 2.1.3 The Exchange-Correlation Functional . . . 12
  - 2.1.4 van der Waals Interactions . . . 12
  - 2.1.5 Solving the Kohn-Sham Equations . . . 13
- 2.2 Structural Optimization . . . 14
  - 2.2.1 Local Minima . . . 14
  - 2.2.2 Vibrational Modes . . . 15
  - 2.2.3 Transition State Theory . . . 15
  - 2.2.4 Energy Barriers . . . 16
  - 2.2.5 Molecular Dynamics . . . 17
  - 2.2.6 Entropy Contributions . . . 18
  - 2.2.7 Adsorption and Desorption . . . 20

3 Kinetic Modeling **21**
- 3.1 The Chemical Master Equation . . . 22
- 3.2 Kinetic Monte Carlo Modeling . . . 25
- 3.3 Comparison between Mean-field and kMC Modeling . . . 26
- 3.4 Analysis of Reaction Kinetics . . . 28

4 Modeling Reactions over Nanoparticles **31**
- 4.1 Scaling Relations . . . 32
  - 4.1.1 Descriptors . . . 32

4.2 Kinetic Coupling 34
4.3 Breaking the Scaling Relations with Alloys 35
4.4 Direct Formation of H_2O_2 35
4.5 Reactions at Solid-Liquid Interfaces 36
4.6 Dynamics of Nanoparticles 39

5 Conclusions **41**
5.1 Limitations 42
5.2 Outlook 43

Acknowledgments **45**

Bibliography **47**

1

Introduction

Heterogeneous catalysis is crucial for a range of environmental purposes, including the after-treatment of exhaust gases from combustion engines [1, 2] and in fuel cell applications [3]. Catalysis is also an indispensable component in the chemical industry, where almost 90 % of all products are produced in catalytic processes [1]. The catalyst offers an alternative reaction path, for which the activation energy of the reaction is decreased, as compared to the reaction without a catalyst. A schematic illustration of the influence of a catalyst is shown in Figure 1.1. The reacting molecules bond to the catalyst surface, and the overall reaction is divided into a set of surface reactions. The surface reactions include the breaking of chemical bonds, diffusion of the intermediates on the catalyst surface, and the formation of new chemical bonds. When the product is formed, it leaves the catalyst surface. The alternative reaction path and decreased activation energy in the presence of the catalyst have important consequences for the reaction, as both the reaction rate and the distribution of the products can be altered [4]. It should be noticed that the catalyst, ideally, is not consumed in the reaction, and the energies of the reactants and products are not influenced by the catalyst. Thus, the catalyst does not alter the thermodynamics of the reaction.

Catalysis can be divided into homogeneous, heterogeneous and bio catalysis, depending on the catalyst and the state of the reactants [1]. In heterogeneous catalysis, reactant molecules in gas or liquid phase react on a solid catalyst. A catalyst is characterized by the rate and the selectivity towards the desired products. Industrially, catalysts are constituted of supported metal(alloy) nanoparticles to provide a large surface area. However, it is generally challenging to discover the most efficient catalyst for a specific catalytic process. The reactants should bind strongly enough to adsorb on the catalyst surface, but simultaneously, the products should

bind weakly enough to desorb after the reaction. This is known as the Sabatier principle [1, 5]. One way to advance the discovery of new, efficient catalysts, is to understand the catalytic processes on the atomic level.

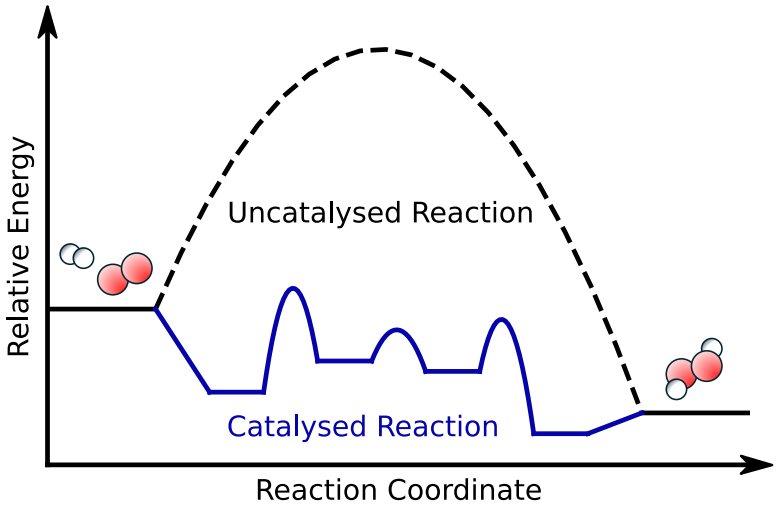

Figure 1.1: A schematic illustration of the influence of a catalyst in a chemical reaction. In the absence of a catalyst, the energy barrier for the reaction is high. On the catalyst surface, an alternative reaction route is enabled, in which the reaction rate is increased.

1.1 Heterogeneous Catalysis

From Berzelius' description of the catalytic force in 1835, to the end of the 1800's, the phenomenological understanding of the influence of reaction conditions and temperature was developed, thanks to the work of *e.g.*, Ostwald and Arrhenius [1]. However, the understanding of the catalysts was based mainly on experimental observations, and the detailed knowledge of the catalytic processes was limited [6]. The understanding of catalytic reactions developed rapidly in the beginning of the 1900's, with understanding of adsorption processes and kinetics of surface reactions [1, 7]. It was discovered that the reactants form chemical bonds with the catalyst surface upon adsorption, and may, thereafter, react with other species on the surface. However, despite the mechanisms in the catalytic reactions being better understood, approximate expressions for the rate of the surface reactions could not be obtained until 1935, when Eyring combined statistical mechanics with quantum mechanical results to predict the rate of the breaking and formation of chemical bonds [8]. The result is known as transition state theory, and is, still,

an important part of the description of catalytic reactions.

The understanding of catalytic processes has developed in parallel with experimental methods, used to characterise the catalytic reactions in different ways. Since the catalytic performance depends on the surface properties of the catalyst, it is natural to investigate the catalyst structure. This was made possible in the beginning of the 1900's, when X-ray diffraction methods were developed to characterise the crystal structure of a catalyst [1]. Probing the surface structure of the catalyst was made possible by other techniques, such as electron microscopy and low-energy electron diffraction. Later, transmission electron microscopy and scanning tunneling microscopy have made it possible to probe the local structure of the surface with atomic resolution [9–11]. However, the structure of the catalyst surface is only one of the important aspects in the characterisation of the catalyst. Another aspect is the chemical state of the catalyst. This property is often probed by X-ray techniques. In X-ray photoelectron spectroscopy, it is possible to obtain information about both the elemental distribution of the catalyst, and the oxidation state of the catalyst [12–14].

To investigate the kinetics of catalytic processes, phenomenological rate expressions could be obtained already in the beginning of the 1900's from measuring reaction rates. However, to understand mechanisms on the catalyst surface, other methods had to be employed. Infrared spectroscopy techniques can be used to investigate which adsorbates are present on the catalyst surface at different reaction conditions. Furthermore, the adsorption energy and the desorption rate from the catalyst surface can be obtained by *e.g.*, microcalorimetry and temperature programmed desorption experiments, respectively [1].

Many of these characterisation techniques with atomic resolution are used on model systems, such as single-crystalline surfaces, at low gas pressure conditions. In industrial applications, where supported nanoparticles are used in harsh reaction conditions, the mechanism and kinetics of the catalytic reaction may differ [1, 15]. To aid the interpretation of experimental results and understand the mechanisms on catalyst surfaces for different reactions at different reaction conditions, quantum mechanical calculations and kinetic simulations could be important.

1.2 Computational Approaches in Catalysis

As the understanding of catalytic reaction mechanisms evolved, it was possible to go deeper than the phenomenological description of overall reaction rates, proposed by Ostwald and Arrhenius. Heterogeneous catalytic reactions are often assumed to

follow the Langmuir-Hinshelwood mechanism [1]. In this mechanism, the overall reaction is divided into adsorption processes, elementary reactions on the surface, and desorption processes. However, even with transition state theory, the elementary reaction rates were difficult to obtain, due to the limited computational power and low accuracy of the electronic structure calculations. Early work was, therefore, concentrated on the understanding of atomic and molecular adsorption processes. From this understanding, it was eventually possible to describe trends in adsorption energy on different metal surfaces [16, 17]. Comparison between calculated adsorption energies and catalytic activity made it later possible to predict catalytic efficiency of different metals from simple descriptors, similar to the Sabatier principle [18, 19].

Thanks to the development of density functional theory calculations with sufficient accuracy in the 1990's [20–22], it is presently possible to calculate the adsorption energies and elementary reaction rates from first-principles. Explicit calculations of the elementary reactions on model surfaces in combination with mean-field kinetic modeling has been employed extensively to describe catalytic reactions [23–27]. In the mean-field approach, the kinetic behavior over one type of catalytic site is described by explicitly solving the kinetic rate equations. While this approach has provided great insights into catalytic reactions over extended surfaces, it breaks down in the description of catalytic reactions over nanoparticles or in the case of more complex reaction mechanisms [28, 29].

Describing the catalytic reactions over nanoparticles is challenging, as the characteristics of the reaction may depend strongly on where on the nanoparticle the reaction occurs [30, 31]. The description becomes even more challenging in the case of alloy particles, where the different metals have different chemical properties, over which the kinetics of the reaction may differ. To describe the catalytic reactions in these cases, it is crucial to take the composition of the catalyst and the abundance of different catalytic sites into consideration. One of these approaches is kinetic Monte Carlo simulations, in which the kinetics of the reaction is investigated in a stochastic approach [32–34]. Kinetic Monte Carlo simulations, based on density functional theory calculations, have been used to describe the kinetics and reveal the governing factors of the efficiency for a range of catalytic reactions [35–38]. However, several challenges still remain to close the gap between the results obtained from kinetic models and experimental observations. Some of these challenges involve the dynamic behavior of the catalyst surface and the influence of complex reaction conditions, such as when the reaction is occurring in an aqueous solution.

1.3 Direct H_2O_2 synthesis from H_2 and O_2

Hydrogen peroxide, H_2O_2, is an important industrial chemical with a variety of uses, including the bleaching of textiles, waste-water treatment and organic synthesis [39–41]. The current production process involves the sequential reduction and oxidation of anthraquinones. The process depends on large scale facilities, and is accompanied by the production of waste, and energy-consuming liquid-liquid extractions [41]. An alternative approach, where H_2O_2 is produced in a direct process, directly from H_2 and O_2, at the location of usage is desirable, as it has the potential to be both energy efficient and cost effective [42, 43]. However, a direct process is challenging, as the formation of H_2O_2 competes with the irreversible $O-O$ bond rupture, leading to the thermodynamically favorable formation of H_2O [44, 45]. A candidate catalyst, which has been intensively studied for the direct formation of H_2O_2 is Pd [46–50]. However, Pd suffers from low selectivity towards H_2O_2, due to the strong interaction between Pd and oxygen, consequently breaking the $O-O$ bonds. Another possible catalyst is Au. However, the activity over Au particles is low [51], as H_2 cannot adsorb and dissociate over Au, except at the interface with the support [52]. Alloys of Pd and Au have shown to be active and selective towards H_2O_2 [51, 53]. In the dilute limit, with Pd monomers resided in the surface of Au nanoparticles, the selectivity has been shown to approach 100 % [54]. The mechanistic understanding of the direct formation of H_2O_2 over dilute PdAu alloys is difficult, as the reaction occurs at the interface between the particles and a water solution. Moreover, the activity and selectivity depend on Pd residing in the surface of dilute PdAu nanoparticles, and not in the bulk of Au, which is thermodynamically preferred in an inert atmosphere [55].

1.4 Objectives

The aim of this thesis is to investigate the kinetics of catalytic reactions from first-principles using kinetic Monte Carlo simulations. Specifically, the direct formation of H_2O_2 from O_2 and H_2 over dilute PdAu nanoparticles in an aqueous solution is studied. The direct synthesis of H_2O_2 is an interesting reaction, as H_2O_2 is an industrially important chemical, that is currently produced via energy-inefficient, environmentally unfriendly methods. Moreover, the reaction contains several general characteristics that are applicable to many other catalytic reactions, including reactions occurring at the metal-water interface and the kinetic coupling between different sites. To investigate the generality of the influence of the metal-water interface, the effects of water are investigated also over other metals. The catalytic efficiency of dilute PdAu alloys with different compositions are investigated, as well as the influence of the reaction conditions. The efficiency of the dilute PdAu cat-

alysts depends on Pd residing in the surface. Therefore, the dynamic behavior of the systems is investigated, using kinetic Monte Carlo simulations. Specifically, the deactivation of the catalyst in an inert atmosphere is compared to the activation in a CO atmosphere. A schematic figure visualizing the content of the appended papers is shown in Figure 1.2.

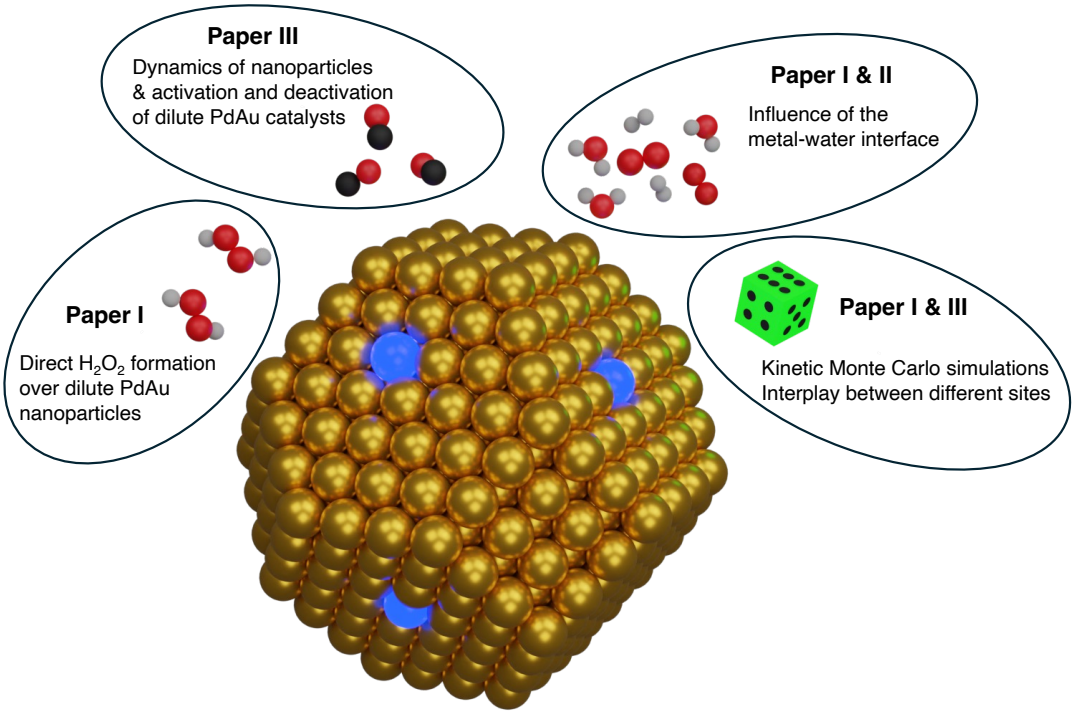

Figure 1.2: A schematic figure visualizing the content in the appended papers.

2

The Potential Energy Surface

The rate of a chemical reaction can phenomenologically be written [1]:

$$r = k \prod_i [A_i]^{n_i}, \tag{2.1}$$

where k is the rate constant, $[A]$ is the activity, such as pressure or concentration, and n is the reaction order. Already in the late 19th century, Arrhenius proposed that the temperature dependence of the rate constant of a chemical reaction could be described by the simple equation [1]

$$k(T) = \nu \mathrm{e}^{-E_a/k_\mathrm{B}T}, \tag{2.2}$$

where ν is a constant, seemingly independent of the temperature, and E_a is the activation energy. Even though this equation was deduced purely from experimental observations, several decades before the birth of quantum mechanics, the equation provides a good description of the behavior of chemical reactions. Today, however, the governing factors of the rate of chemical reactions are better understood, to the point were the rates can be determined from quantum mechanical calculations and kinetic models.

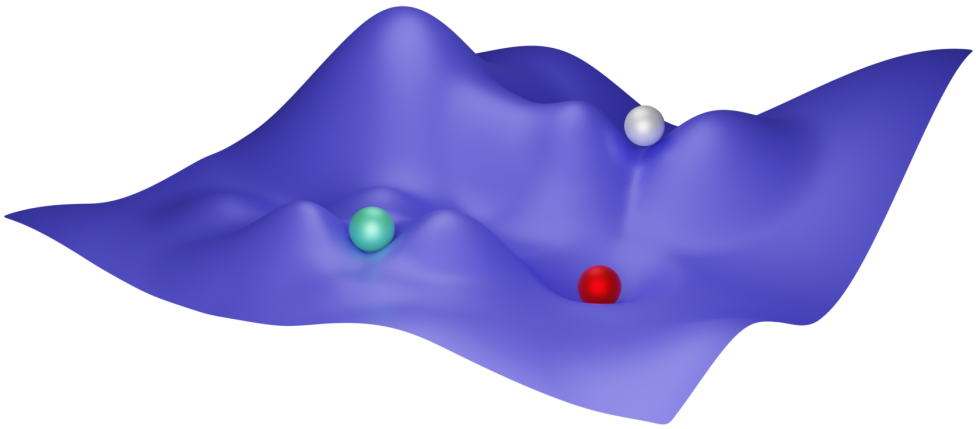

Figure 2.1: A two dimensional potential energy surface. The green ball resides in a local energy minimum, whereas the red ball is located in the global minimum configuration, and the white ball resides in a saddle point.

Reaction kinetics, including the reaction mechanism and elementary reaction rates, are governed by the potential energy surface (PES), Figure 2.1. In a canonical ensemble with a fixed number of particles, fixed volume, and fixed temperature, the changes in Helmholtz free energy

$$\Delta A = \Delta E - T\Delta S \tag{2.3}$$

governs the reaction. If the pressure, instead of the volume, is kept fixed, the changes of Gibbs free energy

$$\Delta G = \Delta H - T\Delta S = \Delta E + P\Delta V - T\Delta S \tag{2.4}$$

steers the reaction. To understand the kinetics of a reaction, it is necessary to know the energies and entropies along the PES. In this work, points on the PES are sampled by density functional theory (DFT) calculations. The entropies are obtained from sampling of the PES in the vicinity of the configuration of interest.

In this section, the methods used to explore the potential energy surface will be presented. This includes a brief introduction to quantum mechanics and DFT. Since DFT is used to sample points at the potential energy surface, methods to explore other points along important paths are also described. The methods include the search for local and global minima, transition states, and how to obtain the free energies.

2.1 The Schrödinger Equation

To calculate the energy of a quantum mechanical system, the stationary (time-independent), Schrödinger equation

$$H\Psi = E\Psi \tag{2.5}$$

has to be solved. Here, H is the Hamiltonian of the system, Ψ is the wave function and E is the energy. In the absence of external fields, the Hamiltonian for a chemical system is the sum of the kinetic energy operators T, and the potential energy operators, V, stemming from the Coulomb interactions, *i.e.*,

$$H = T_{\mathrm{N}} + T_{\mathrm{e}} + V_{\mathrm{NN}} + V_{\mathrm{ee}} + V_{\mathrm{Ne}} = \tag{2.6}$$

$$-\sum_m \frac{\hbar^2}{2M_m}\nabla_m^2 - \sum_i \frac{\hbar^2}{2m_{\mathrm{e}}}\nabla_i^2 + \frac{e^2}{4\pi\varepsilon_0}\sum_m \sum_{n<m} \frac{Z_m Z_n}{|\mathbf{R}_m - \mathbf{R}_n|} + \tag{2.7}$$

$$\frac{e^2}{4\pi\varepsilon_0}\sum_i \sum_{j<i} \frac{1}{|\mathbf{r}_i - \mathbf{r}_j|} - \frac{e^2}{4\pi\varepsilon_0}\sum_m \sum_i \frac{Z_m}{|\mathbf{R}_m - \mathbf{r}_i|}, \tag{2.8}$$

where $\mathbf{R}$ and $\mathbf{r}$ are the positions of the nuclei with mass M and atomic number Z, and the electrons with mass m_{e}, respectively. It is difficult to solve the Schrödinger equation, and analytical solutions exist only for systems with a single electron. For systems with more than one electron, approximations need to be applied. Henceforth, the operators will be expressed in atomic Hartree units, where $\hbar = 4\pi\varepsilon_0 = m_{\mathrm{e}} = e = 1$.

2.1.1 The Born-Oppenheimer Approximation

A first approach to ease the difficulty of finding solutions to the Schrödinger equation for a given chemical system, is to express the wave function of the system as a product between the nucleic wave function and the electronic wave function ($\Psi_{\mathrm{N}}\Psi_{\mathrm{e}}$). In the Born-Oppenheimer approximation, the motions of the electrons and the motions of the nuclei are treated as decoupled [56]. Owing to the small ratio between the mass of an electron and the mass of a nucleus, the nuclei are treated as classical particles, whereas the electrons instantly adjust to the slow variations of the nuclear positions. Hence, the electrons will stay in the same adiabatic eigenstate. This approximation yields small errors, as long as the nuclei are slowly moving and the electronic energy levels are sufficiently separated.

When invoking the Born-Oppenheimer approximation, the electronic Schrödinger equation

$$H_{\mathrm{e}}\Psi_{\mathrm{e}}(\mathbf{r}_1, ..., \mathbf{r}_N) = E_{\mathrm{e}}\Psi_{\mathrm{e}}(\mathbf{r}_1, ..., \mathbf{r}_N) \tag{2.9}$$

is solved to obtain the electronic energy of the system. In this case, Ψ_{e} is the electronic wave function, which depends on the electron positions $\mathbf{r}$, in which the spin of the electron, σ, is included. E_{e} is the electronic energy of the system, and H_{e} is the electronic Hamiltonian:

$$H_{\mathrm{e}} = T + V_{\mathrm{ee}} + V_{\mathrm{ext}}, \tag{2.10}$$

where $V_{\mathrm{ext}} = V_{\mathrm{Ne}}$ for a chemical system in the absence of other fields.

2.1.2 The Electronic Density

An early approach to solve the electronic Schrödinger equation was suggested by Hartree in the beginning of the 20th century [57]. It was proposed that the many-electron wave function could be approximated as the product of the single-electron wave functions *i.e.*,

$$\Psi_{\mathrm{e}}(\mathbf{r}_1, ..., \mathbf{r}_N) = \psi_1(\mathbf{r}_1) \cdots \psi_N(\mathbf{r}_N). \tag{2.11}$$

With this approach, each particle is subject to a single-electron wave equation

$$\big(-\frac{1}{2}\nabla^2 + v_{\mathrm{ext}} + \bar{v}_{\mathrm{ee},i}\big)\psi_i(\mathbf{r}) = \varepsilon_i \psi_i(\mathbf{r}) \tag{2.12}$$

where v_{ext} is the external potential, and $\bar{v}_{ee}$ is an electronic potential, derived from the mean electronic potential from the other electrons. With this approach, the energy can be obtained in an iterative process. A significant problem with Eq. (2.12) is that the obtained one-electron wave functions are not orthogonal, and the many electron wave function is not antisymmetric with respect to the interchange of two electrons. Fock and Slater later proposed that, instead of the product, the many-electron wave function could be obtained from the single-electron wave functions via the determinant. This approach captures the anti-symmetric properties of the fermionic wave function, and the one-electron wave functions are orthogonal.

Thomas and Fermi proposed an alternative approach, where instead of using single-particle wave functions, the electron density is used. This approach was later developed by Hohenberg and Kohn [58], showing that there exists a universal functional F, independent of the external potential, that maps the electron density of the system to the electronic energy of the system, *i.e.*,

$$E[n(\mathbf{r})] = \int n(\mathbf{r}) v_{\mathrm{ext}}(\mathbf{r}) \mathrm{d}\mathbf{r} + F[n(\mathbf{r})] = E_{\mathrm{ext}}[n(\mathbf{r})] + F[n(\mathbf{r})] \tag{2.13}$$

where $n(\mathbf{r})$ is the electron density. Furthermore, the energy functional, E, obeys the variational principle; the ground state energy of the system is obtained from the

ground state electron density. The functional F can be separated into two different functionals, where one is due to the classical Coulomb interaction between the electrons and G is a universal functional:

$$E[n(\mathbf{r})] = E_{\text{ext}}[n(\mathbf{r})] + \frac{1}{2}\int n(\mathbf{r})v_{\text{ee}}(\mathbf{r})\mathrm{d}\mathbf{r} + G[n(\mathbf{r})] \tag{2.14}$$

$$= E_{\text{ext}}[n(\mathbf{r})] + E_{\text{ee}}[n(\mathbf{r})] + G[n(\mathbf{r})]. \tag{2.15}$$

Since the electron density is considered, the potential terms take the form

$$v_{\text{ext}}(\mathbf{r}) = -\sum_m \frac{Z_m}{|\mathbf{r} - \mathbf{R}_m|} \tag{2.16}$$

$$v_{\text{ee}}(\mathbf{r}) = \int \frac{n(\mathbf{r}')}{|\mathbf{r} - \mathbf{r}'|}\mathrm{d}\mathbf{r}'. \tag{2.17}$$

This method was, however, difficult to apply, until Kohn and Sham proposed the use of single-particle wave functions [59], orbitals, such that the electron density could be expressed as

$$n(\mathbf{r}) = \sum_i |\psi_i(\mathbf{r})|^2. \tag{2.18}$$

Furthermore, the universal functional G was separated into a kinetic energy operator T_0 for a system of non-interacting electrons with density $n(\mathbf{r})$, and an energy functional E_{xc} to capture the exchange and correlation effects. The kinetic energy of the non-interacting electrons is calculated from the orbitals according to

$$T_0 = -\frac{1}{2}\sum_i \int \psi_i^* \nabla^2 \psi_i. \tag{2.19}$$

The total electronic energy functional is in the Kohn-Sham formulation expressed as

$$E[n(\mathbf{r})] = E_{\text{ext}}[n(\mathbf{r})] + E_{\text{ee}}[n(\mathbf{r})] + T_0[n(\mathbf{r})] + E_{\text{xc}}[n(\mathbf{r})]. \tag{2.20}$$

Owing to the separation of Kohn and Sham, the ground state electronic energy and the ground state electron density of a system can be solved in an iterative approach, similar to the method proposed by Hartree and Fock. The one-electron Kohn-Sham equations take the form

$$(-\frac{1}{2}\nabla^2 + v_{\text{eff}})\psi_i(\mathbf{r}) = \varepsilon_i \psi_i(\mathbf{r}) \tag{2.21}$$

where

$$v_{\text{eff}} = v_{\text{ext}} + v_{\text{ee}} + v_{\text{xc}}, \quad v_{\text{xc}} = \frac{\delta E_{\text{xc}}[n(\mathbf{r})]}{\delta n(\mathbf{r})}. \tag{2.22}$$

The electronic energy of the system is obtained from the eigenvalues of the Kohn-Sham equations and the electron density as

$$E = \sum_{i=1} \varepsilon_i - E_{\text{ee}}[n(\mathbf{r})] + E_{\text{xc}}[n(\mathbf{r})] - \int n(\mathbf{r}) v_{\text{xc}} \mathrm{d}\mathbf{r}. \tag{2.23}$$

2.1.3 The Exchange-Correlation Functional

The exchange and correlation functional E_{xc} should capture exchange and correlation effects omitted *e.g.*, the correlation hole, and the self-interaction in the electron-electron repulsion [60]. A first approach to estimate the exchange and correlation energy effects is to treat the electron density as a locally uniform electron gas with density $n(\mathbf{r})$, with $\varepsilon_{\text{xc}}^{\text{uniform}}$ being the exchange and correlation energy per particle. The exchange and correlation energy functional takes, in this local density approximation (LDA) the form

$$E_{\text{xc}}^{\text{LDA}}[n(\mathbf{r})] = \int n(\mathbf{r})\varepsilon_{\text{xc}}^{\text{uniform}}(n(\mathbf{r}))\mathrm{d}\mathbf{r}. \tag{2.24}$$

The local density approximation can be improved to also take electronic spin into consideration, known as the local spin density approximation:

$$E_{\text{xc}}^{\text{LSDA}}[n_{\uparrow}(\mathbf{r}), n_{\downarrow}(\mathbf{r})] = \int n(\mathbf{r})\varepsilon_{\text{xc}}^{\text{uniform}}(n_{\uparrow}(\mathbf{r}), n_{\downarrow}(\mathbf{r}))\mathrm{d}\mathbf{r} \tag{2.25}$$

where the total electron density $n(\mathbf{r}) = n_{\uparrow}(\mathbf{r}) + n_{\downarrow}(\mathbf{r})$. The local density approximation is adequate when the electron density is slowly varying. However, to better describe varying electronic densities, the gradients of the electron density should be accounted for. One of these functionals is the generalized gradient approximation, where the exchange-correlation energy takes the form

$$\begin{aligned} &E_{\text{xc}}^{\text{GGA}}[n_{\uparrow}(\mathbf{r}), n_{\downarrow}(\mathbf{r})] = \\ &\int n(\mathbf{r})\varepsilon_{\text{xc}}^{\text{uniform}}(n_{\uparrow}(\mathbf{r}), n_{\downarrow}(\mathbf{r}))F_{\text{xc}}[n_{\uparrow}(\mathbf{r}), n_{\downarrow}(\mathbf{r}), \nabla n_{\uparrow}(\mathbf{r}), \nabla n_{\downarrow}(\mathbf{r})]\mathrm{d}\mathbf{r} \end{aligned} \tag{2.26}$$

where F_{xc} is an enhancement functional that determines the magnitude of the exchange and correlation contributions at a given point, as a functional of the electron density and its gradient. In principle, higher order gradient expansions can also be included.

2.1.4 van der Waals Interactions

For some chemical systems, such as the physisorption of a molecule to a catalyst surface, the structure depends on long-range van der Waals interactions [1]. The interactions do not stem from orbital overlap, but from dipole fluctuations in the electronic density, resulting in electric-field coupling. Generalized gradient approximation exchange-correlation functionals do not capture van der Waals interactions, and other functionals capturing these interactions have been developed [61]. A simpler approach to capture the van der Waals interactions is with an ad-hook

approach, where the van der Waals interactions are calculated from the electron density, *i.e.*, outside the iterative Kohn-Sham loop [62, 63]. This is a time-effective approach, that corrects some of the flaws of the generalized gradient approximations.

2.1.5 Solving the Kohn-Sham Equations

According to Bloch's theorem, the electronic wave function in a periodic external potential can be expressed as: [60]

$$\psi_{\mathbf{k}}(\mathbf{r}) = \mathrm{e}^{i\mathbf{k}\cdot\mathbf{r}} u_{\mathbf{k}}(\mathbf{r}) \tag{2.27}$$

where $\mathbf{k}$ is the wave vector, and $u_{\mathbf{k}}(\mathbf{r})$ has the same periodicity as the potential. This makes it possible to express the wave function as a Fourier series:

$$\psi_{\mathbf{k}}(\mathbf{r}) = \mathrm{e}^{i\mathbf{k}\cdot\mathbf{r}} \sum_{\mathbf{G}} C_{\mathbf{k}+\mathbf{G}} \mathrm{e}^{i\mathbf{G}\cdot\mathbf{r}}. \tag{2.28}$$

The wave function of the orbital can, therefore, be calculated by only considering the Brillouin zone. The expansion of the Kohn-Sham orbitals are often truncated, due to the decreasing nature of the Fourier coefficients, to a given value E_{cut}, such that

$$\frac{1}{2}|\mathbf{k}+\mathbf{G}|^2 < E_{\mathrm{cut}}. \tag{2.29}$$

Fortunately, it is not necessary to sample the entire Brillouin zone, but rather a specific number of $\mathbf{k}$ vectors. The number and distribution of the $\mathbf{k}$ vectors has to be determined as to when the electronic energy of the system is converged. The total electronic density can then be expressed from the wave functions obtained from each $\mathbf{k}$ vector as

$$n(\mathbf{r}) = \sum_{\mathbf{k}} \omega_{\mathbf{k}} \sum_{i} |\psi^i_{\mathbf{k}}(\mathbf{r})|^2 \tag{2.30}$$

where $\omega_{\mathbf{k}}$ is the weight factor of each $\mathbf{k}$ vector in the Brillouin zone, and the second sum is taken over all eigenfunctions from the Kohn-Sham equations.

In practice, the Kohn-Sham equations are not solved by complete sampling of a three dimensional grid, but rather by the use of some basis set, *e.g.*, local orbitals or plane waves. In the plane waves approach, the wave function is expressed as a linear combination of plane waves in the reciprocal space, derived from its Fourier transform [60]. The Fourier coefficients in the linear combination and the energy eigenvalues are thereafter obtained by solving the Kohn-Sham equations in reciprocal space. There are, however, problems when applying a plane wave basis set; it is only possible to apply plane waves when the potential is shallow, or relatively

smooth. Close to the nuclei the wave function could be rapidly oscillating, and a large number of plane waves would be required to obtain accurate results. An approach to solve this issue is the frozen core projector augmented waves method [64]. In this approach, the electrons close to the nuclei are considered frozen. The wave functions of the electrons outside the core are described by pseudo-plane waves $|\tilde{\phi}\rangle$, which can be translated into the regular plane waves by a linear transformation operator T. It is then straight forward to solve the Kohn-Sham equations with the pseudo-plane waves:

$$T^{\dagger}HT\,|\tilde{\phi}\rangle = \varepsilon T^{\dagger}T\,|\tilde{\phi}\rangle \tag{2.31}$$

where ε is the energy eigenvalue of the one electron Kohn-Sham equation. The one-electron wave functions are obtained from the pseudo wave functions as

$$|\psi\rangle = |\tilde{\psi}\rangle + \sum_i (|\phi_i\rangle - |\tilde{\phi}_i\rangle)\,\langle\tilde{p}_i|\tilde{\psi}\rangle \tag{2.32}$$

where $\langle\tilde{p}|$ is a projector function satisfying $\langle\tilde{p}_i|\tilde{\phi}_j\rangle = \delta_{ij}$.

2.2 Structural Optimization

The catalyst, molecules, and species adsorbed on the catalyst surface will most of the time reside in their lowest energy configurations. The reaction rate constant of an elementary reaction depends on the energy difference between a minimum energy configuration and the energy of the transition state in the potential energy surface. Therefore, it is important to find global and local minima, and transition states in the potential energy surface. In the DFT calculations described in 2.1, only the ground state electronic structure for given positions of the nuclei are solved, *i.e.*, one point in the potential energy surface. Hence, methods must be used to probe the potential energy surface, to find minima and transition state configurations. The potential energy surface needs to be probed also to obtain the entropy contributions for specific states in the catalytic reaction.

2.2.1 Local Minima

To find local minimum structures, the nucleic positions are relaxed according to the forces acting on each nuclei. It is with DFT calculations possible to obtain the forces acting on each nuclei, directly from the ground state electron density and the positions of the nuclei. Using the Hellmann-Feynman theorem, the forces acting on nuclei i is given by

$$\mathbf{F}_i = -\nabla_i\left(\int n(\mathbf{r})v_{\text{ext}}\mathrm{d}\mathbf{r} + \sum_m \sum_{n<m} \frac{Z_m Z_n}{|\mathbf{R}_m - \mathbf{R}_n|}\right). \tag{2.33}$$

The nucleic positions can, thereafter, be updated according to the forces and new electronic structure calculations can be performed.

2.2.2 Vibrational Modes

To calculate the Gibbs free energy differences for elementary reactions, the entropies of the different states must be calculated from the PES. Atoms and molecules bound to a catalyst surface vibrate with characteristic frequencies, depending on the potential energy surface in the vicinity of the specie. The energy levels of the vibrations are quantized as

$$E_n = hf\left(\frac{1}{2} + n\right), \quad n = 0, 1, 2, ... \tag{2.34}$$

Knowledge about the character of the vibrational modes can give important information of the chemical bonds. For an adsorbate on a catalyst surface, in a local minimum, all eigenvalues are positive. For a free translation, the eigenvalue is zero, whereas at a transition state (a saddle point in the PES) exactly one eigenvalue is imaginary. In this work, the vibrational modes have been calculated using the harmonic approximation. The potential energy surface at the vicinity of the specie of interest is approximated as a quadratic function. A mass-weighted Hessian is obtained by finite movements of the nuclei. The vibrational frequencies are thereafter calculated from the eigenvalues of the Hessian as $f_i = \sqrt{\lambda_i}/2\pi$. Similarly, the eigenvectors of the Hessian correspond to the atomic displacements for the vibration.

2.2.3 Transition State Theory

Consider an elementary reaction, *e.g.*,

$$A \rightleftharpoons A^{\ddagger} \rightarrow B, \tag{2.35}$$

where $A^{\ddagger}$ is the transition state of the reaction. The transition state is the lowest energy saddle point in the potential energy surface. The reaction rate constant of the reaction is given from the probability of the specie being at the transition state compared to the initial state via a quasi-equilibrium, and the frequency along the reaction coordinate [8],

$$k_{A\rightarrow B} = f\frac{Q_A^{\ddagger}}{Q_A} \tag{2.36}$$

where Q are the partition functions, and f is the vibrational frequency along the reaction coordinate. The contribution of the vibrational frequency along the reaction

coordinate can be extracted from the partition function quota, *i.e.*,

$$k_{A\to B} = f\frac{\mathrm{e}^{-hf/2k_\mathrm{B}T}}{1-\mathrm{e}^{-hf/k_\mathrm{B}T}}\frac{Q_A^{\ddagger,*}}{Q_A}. \tag{2.37}$$

Under the assumption that $k_\mathrm{B}T >> hf$, the partition function of the reaction coordinate can be approximated by a first order Taylor expansion, yielding the rate constant

$$k_{A\to B} = \frac{k_\mathrm{B}T}{h}\frac{Q_A^{\ddagger,*}}{Q_A}. \tag{2.38}$$

If the energies of the initial state and transition state are extracted from the partition functions, the final expression for the rate constant becomes

$$k_{A\to B} = \frac{k_\mathrm{B}T}{h}\frac{Q_{A,0}^{\ddagger,*}}{Q_A}\mathrm{e}^{-\Delta E^\ddagger/k_\mathrm{B}T}, \tag{2.39}$$

where $\Delta E^\ddagger$ is the energy difference between the transition state and the initial state. Note that this is the rate constant of the reaction.

2.2.4 Energy Barriers

The rate of the formation of B is expressed as

$$r_{A\to B} = \frac{\mathrm{d}B}{\mathrm{d}t} = k_{A\to B}[A], \tag{2.40}$$

where $[A]$ is the activity of A, *e.g.*, coverage, pressure or concentration. The reaction order in Eq. (2.1) is in this case 1. In the rate constant, the energy of the initial state and the partition function can be obtained from DFT calculations and vibrational analysis. To find the saddle point in the potential energy surface, several techniques could be applied. A common approach is to use the nudged elastic band method [65]. Between the local minima, the initial state and the final state configurations, $N-1$ intermediate configurations are created. Between the $N+1$ configurations, N springs are invoked. During the calculation, the initial and final structures are fixed in their positions. Along the reaction coordinate, the intermediate structure i is optimized from the force stemming from the potential energy surface perpendicular to the reaction coordinate and the spring force along the reaction coordinate, *i.e.*,

$$\mathbf{F}_{i,\mathrm{tot}} = \mathrm{F}_{i,\parallel}^{\mathrm{spring}} - \nabla E(\mathbf{R}_i)_\perp. \tag{2.41}$$

Along the normalized reaction coordinate for each structure $\hat{\mathbf{r}}_{i,\mathrm{reaction}}$, the spring force along the coordinate and the perpendicular force from the potential energy

surface are calculated as

$$\nabla E(\mathbf{R}_i)_\perp = \nabla E(\mathbf{R}_i) - \nabla E(\mathbf{R}_i) \cdot \hat{\mathbf{r}}_{i,\text{reaction}} \hat{\mathbf{r}}_{i,\text{reaction}} \tag{2.42}$$

$$\mathbf{F}_{i,\parallel}^{\text{spring}} = k_{\text{spring}}(|\mathbf{R}_{i+1} - \mathbf{R}_i| - |\mathbf{R}_i - \mathbf{R}_{i-1}|)\hat{\mathbf{r}}_{i,\text{reaction}}, \tag{2.43}$$

where k_{spring} is the spring force of the elastic band. However, this method often suffers from difficulties in finding the exact configuration of the saddle point in the potential energy surface. A better approach to obtain estimates for the saddle point is the climbing-image nudged elastic band method [66]. In this approach, the highest energy structure is not affected by the springs, but only the forces obtained from the potential energy surface. However, since the transition state is a maximum energy configuration along the reaction coordinate, the tangential forces acting on the structure are inverted, *i.e.*,

$$\mathbf{F}_{\text{tot}} = -\nabla E(\mathbf{R}) + 2\nabla E(\mathbf{R}) \cdot \hat{\mathbf{r}}_{\text{reaction}} \hat{\mathbf{r}}_{\text{reaction}}. \tag{2.44}$$

2.2.5 Molecular Dynamics

Another way of finding both minimum energy structures and transition state structures is the use of molecular dynamics simulations. By integrating Newton's equations of motion, the time-evolution of a system can be investigated. The integration can be done in several ways. However, an approach where the velocities and positions are updated using the trapezoidal rule is common [67]. The system is evolved with time step Δt for each particle i according to:

$$\mathbf{v}_i\left(t + \frac{\Delta t}{2}\right) = \mathbf{v}_i\left(t - \frac{\Delta t}{2}\right) + \frac{\mathbf{F}_i}{m_i}\Delta t \tag{2.45}$$

$$\mathbf{r}_i\left(t + \Delta t\right) = \mathbf{r}_i(t) + \mathbf{v}_i\left(t + \frac{\Delta t}{2}\right)\Delta t \tag{2.46}$$

$$\text{and} \quad \mathbf{v}_i(t) = \frac{1}{2}\left(\mathbf{v}_i\left(t + \frac{\Delta t}{2}\right) + \mathbf{v}_i\left(t - \frac{\Delta t}{2}\right)\right) \tag{2.47}$$

where the forces $\mathbf{F}$ are obtained from DFT calculations. Molecular dynamics simulation will often sample local minima in the potential energy surface, since the forces is merely the gradient of the potential energy surface. Therefore, to sample improbable configurations, *e.g.*, configurations close to a transition state, during finite simulation times, other methods has to be applied [68]. A common approach is to constrain positions during the molecular dynamics simulation. To study transition state configurations, it is often convenient to constrain bond lengths between species on the surface. If constraints are invoked, the velocities are updated according to a total force, stemming from the forces due to the potential energy surface,

and the force of the constraint:

$$\mathbf{F}_{i,\text{constraint}} = -\sum_k \lambda_k \nabla_i \sigma_k, \tag{2.48}$$

where the summation is over all constraints σ, and λ is the Lagrange multiplier associated with the constraint [69]. Since catalytic reactions are governed by changes in free energy, the electronic energy always needs to be complemented by entropy contributions. The use of molecular dynamics simulations, makes it possible to obtain also the entropy contributions. One approach is to sample the configuration space of interest and obtain the partition function. A more direct approach is to combine constrained molecular dynamics simulations with the blue-moon ensemble method [70]. The changes in Helmholtz free energy can in this case be obtained directly from the simulation, albeit at a high computational cost due to the data required to get converged results. In this case, it is possible to perform thermodynamic integration from the gradient of the free energy at a specific constrain as

$$\left(\frac{\partial A}{\partial \xi}\right)_{\xi^*} = \frac{\langle Z^{-1/2}(-\lambda + k_\text{B}TG)\rangle_{\xi^*}}{\langle Z^{-1/2}\rangle_{\xi^*}}, \tag{2.49}$$

where λ is the Lagrange multiplier associated with the constraint, and

$$Z = \sum_i \frac{1}{m_i}(\nabla_i \xi)^2 \tag{2.50}$$

$$G = \frac{1}{Z^2}\sum_{i,j}\frac{1}{m_i m_j}(\nabla_i \xi)\cdot\nabla_i(\nabla_j\xi)\cdot(\nabla_j\xi). \tag{2.51}$$

The parameter ξ is, for example, the bond length between two species, *i.e.*, $\xi = |\mathbf{r}_i - \mathbf{r}_j|$. This approach is convenient when investigating free energy barriers of rare events in a highly dynamic system, where nudged elastic band calculations in combination with vibrational analysis is not sufficient.

2.2.6 Entropy Contributions

For adsorbates chemisorbed to a metal surface, all movements can often be approximated as vibrations. The partition function for a specie with i vibrational modes is

$$Q_\text{vibration} = \prod_i \sum_{n=0}^{\infty} \mathrm{e}^{-E_{i,n}/k_\text{B}T} = \exp\left(-\frac{1}{2k_\text{B}T}\sum_i hf_i\right)\prod_i \frac{1}{1-\mathrm{e}^{-hf_i/k_\text{B}T}}. \tag{2.52}$$

The sum $\frac{1}{2}\sum_i hf_i$ is known as the zero-point energy. Since DFT calculations provide energies at the bottom of the vibrational energy well, the zero-point energy

is often considered as part of the energy contribution, rather than a part of the partition function.

The entropy contribution follows from the partition function as

$$S = \frac{\partial}{\partial T}(k_{\mathrm{B}} T \ln Q). \tag{2.53}$$

The situation is different when a specie can also rotate or translate, as in the cases of gas phase molecules or adsorbates translating over a catalyst surface. The contributions to the partition function can be considered to be decoupled, and the total partition function is given from the product of the different contributions, *i.e.*,

$$Q = Q_{\mathrm{translation}} Q_{\mathrm{rotation}} Q_{\mathrm{vibration}} Q_{\mathrm{e}} Q_{\mathrm{N}}. \tag{2.54}$$

The last partition functions, Q_{e} and Q_{N}, are due to the electronic states and the nucleic states, respectively, and can often be set to unity. The translational partition function is derived from the energy levels for a particle in a box,

$$Q_{\mathrm{translation}} = \sum_s \mathrm{e}^{-E(s)/k_{\mathrm{B}}T} = \sum_{n_x}\sum_{n_y}\sum_{n_z} \mathrm{e}^{-\frac{h^2}{8mk_{\mathrm{B}}T}\left(\frac{n_x^2}{L_x^2}+\frac{n_y^2}{L_y^2}+\frac{n_z^2}{L_z^2}\right)} \tag{2.55}$$

$$\approx \int_0^\infty \mathrm{d}n_x \int_0^\infty \mathrm{d}n_y \int_0^\infty \mathrm{d}n_z \, \mathrm{e}^{-\frac{h^2}{8mk_{\mathrm{B}}T}\left(\frac{n_x^2}{L_x^2}+\frac{n_y^2}{L_y^2}+\frac{n_z^2}{L_z^2}\right)} \tag{2.56}$$

$$= V\left(\frac{\sqrt{2\pi m k_{\mathrm{B}} T}}{h}\right)^3 \tag{2.57}$$

The rotational partition function is more difficult, since it differs between different dimensions of rotation, according to

$$Q_{\mathrm{rotation}} = \begin{cases} \frac{2\pi}{h}\sqrt{2\pi I k_{\mathrm{B}} T}, & \text{if 1 dimensional rotation,} \\ \frac{8\pi^2 I k_{\mathrm{B}} T}{\sigma h^2}, & \text{if 2 dimensional rotation,} \\ \frac{\sqrt{\pi}}{\sigma}\prod_i \sqrt{\frac{8\pi^2 I_i k_{\mathrm{B}} T}{h^2}}, & \text{if 3 dimensional rotation.} \end{cases} \tag{2.58}$$

I and I_i are the moment of inertia and the eigenvalues to the matrix consisting of the moments of inertia, respectively. σ is a symmetry factor, which is 2 if the molecule has an inversion centre and 1 otherwise. The partition function also has important consequences when analysing the probabilities between different states. The probability of a specie being in a specific state s_k is

$$p(s_k) = \frac{g(s_k)\mathrm{e}^{-E(s_k)/k_{\mathrm{B}}T}}{\sum_s g(s)\mathrm{e}^{-E(s)/k_{\mathrm{B}}T}}, \tag{2.59}$$

where $g(s)$ is the degeneracy of state s. This is known as the Boltzmann-distribution.

2.2.7 Adsorption and Desorption

Two important elementary reactions are adsorption and desorption. The adsorption rate can be derived from the partition functions and transition state theory. At the transition state of the adsorption, the molecule can translate freely in two dimensions, instead of in three dimensions as in the gas phase. Hence, the adsorption rate constant is

$$k_{\text{ads}} = \frac{k_{\text{B}}T}{h}\frac{Q^{\ddagger}_{\text{2D}}}{Q_{\text{3D}}}\text{e}^{-\Delta E^{\ddagger}/k_{\text{B}}T} = \frac{pA}{\sqrt{2\pi m k_{\text{B}}T}}\text{e}^{-\Delta E^{\ddagger}/k_{\text{B}}T}. \tag{2.60}$$

However, due to *e.g.* geometric effects and spin effects that are not captured when applying the Born-Oppenheimer approximation in transition state theory, the rate must sometimes be scaled by a sticking coefficient, s_0. In these cases, the expression for the adsorption rate constant is:

$$k_{\text{ads}} = \frac{s_0 pA}{\sqrt{2\pi m k_{\text{B}}T}}\text{e}^{-\Delta E^{\ddagger}/k_{\text{B}}T}. \tag{2.61}$$

At equilibrium conditions, the desorption rate is obtained from the adsorption rate and the equilibrium constant, K:

$$K = \text{e}^{-\Delta G/k_{\text{B}}T} = \frac{k_{\text{ads}}}{k_{\text{des}}} \implies k_{\text{des}} = k_{\text{ads}}\text{e}^{\Delta G/k_{\text{B}}T}, \tag{2.62}$$

where ΔG is the change in Gibbs free energy upon adsorption.

3

Kinetic Modeling

Kinetic models are often crucial to properly understand a catalytic reaction, including the reaction mechanism, and possible kinetic bottlenecks [71]. In kinetic models, the free energies are used to describe the time evolution of the reaction, and how the reaction depends on reaction conditions, such as temperature and partial pressures. A catalytic reaction can be divided into a set of elementary reactions. A schematic representation of the elementary reactions for the reaction $A + \frac{1}{2} B_2 \rightleftharpoons AB$ is shown in Figure 3.1. The elementary reactions include adsorption and desorption processes (red and blue arrows) and diffusion processes (black arrows), in which the adsorbed species move between different catalytic sites. These elementary reactions, despite not being visible in the overall reaction, are important for the catalytic performance. To form AB over the catalyst surface, B_2 must dissociate, forming 2B (light blue arrows). Once the diatomic molecule has dissociated, it can react with other species on the surface. In Figure 3.1 the reaction between A and B, forming AB, is represented by a green arrow. The formation of the desired product is, in many cases, reversible. Therefore, to emphasise the reversibility of many elementary reactions over a catalyst, the reverse reaction of the formation of AB is also visualized, represented with a green arrow.

In this chapter, an introduction to kinetic modeling is presented. This includes theory about catalytic reactions, mean-field kinetic modeling and kinetic Monte Carlo simulations. Kinetic Monte Carlo (kMC) simulations is a stochastic approach to solve for the time-evolution of a catalytic reaction [33]. Various kinetic Monte Carlo methods exist to integrate the kinetic equations, and in this chapter, the first reaction method is described. Key differences between the mean-field approximation, and kinetic Monte Carlo simulations, are highlighted. The chapter is concluded with a description of kinetic data analysis.

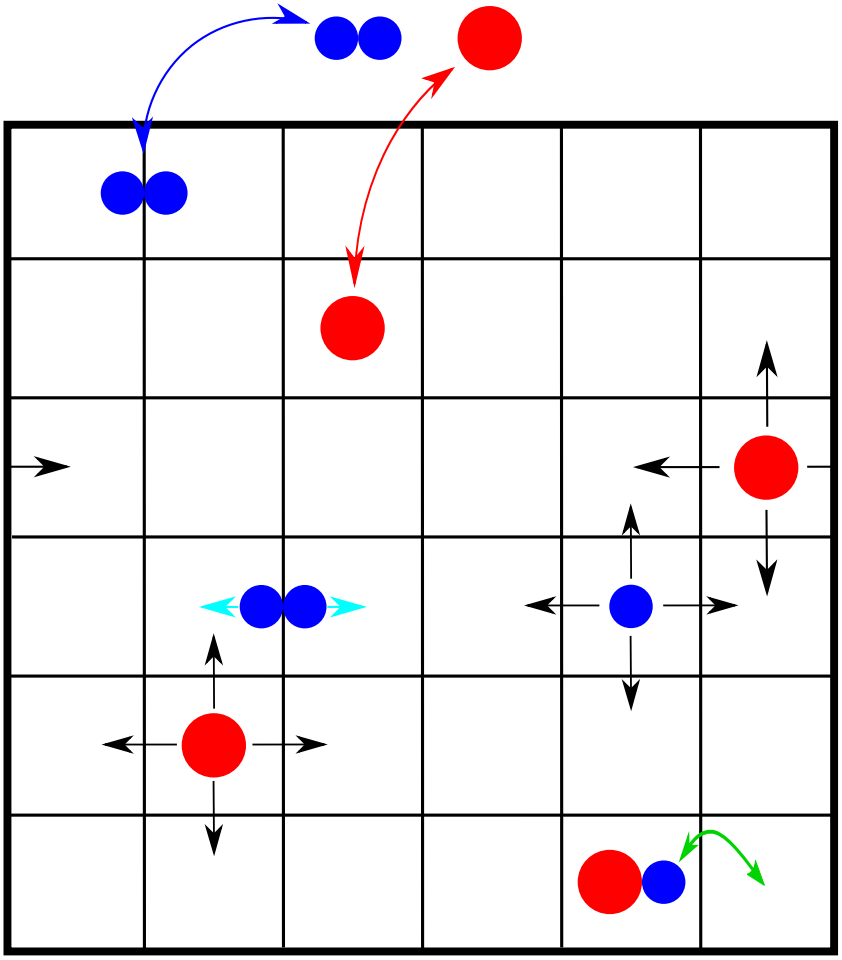

Figure 3.1: A schematic representation of the elementary reactions in the catalytic reaction, where A and $\frac{1}{2}\,B_2$ reacts to form AB. The blue and red arrows represent the adsorption and desorption of A and B_2 on the catalyst surface. The light blue arrows symbolize the dissociation of B_2 on the surface, forming $2\,B$. Green arrows are representing the forward and backward formation of AB, *i.e.*, $A + B \rightleftharpoons AB$. Diffusion of the species are represented with black arrows.

3.1 The Chemical Master Equation

The representation shown in Figure 3.1 is one of the possible arrangements of adsorbates on the catalyst surface. After any surface process, such as an adsorption or desorption event, diffusion process or reaction event, a new state is obtained. The number of possible configurations is large, and therefore difficult to sample. It is, thus, important to explore the configurations in a systematic way. It is possible to derive the time derivative of the probability of a system being in state i, resulting

in the chemical master equation [72]

$$\frac{\mathrm{d}P_i}{\mathrm{d}t} = \sum_j \left[W_{ij}P_j - W_{ji}P_i\right]. \tag{3.1}$$

Here, the sum is taken over the probability of all configurations transferring the system to state i, with rate constant W_{ij}, and the probability of all states that state i could be transferred to, with rate constant W_{ji}. It is also possible to perform the summation over all configurations. However, not all states could transfer the system to state i, or be obtained from state i. Therefore, the transition rates are, for a large number of transitions, zero.

The chemical master equation, together with the rate constants described in the previous chapter, provide the description of the time evolution of a catalytic reaction. However, describing the time evolution of a specific reaction is difficult. The time evolution can, however, in simple cases be solved analytically [33]. The average number of surface specie A adsorbed on the catalyst surface is given by

$$\langle A\rangle = \sum_i P_i A_i, \tag{3.2}$$

where A_i is the number of A adsorbed on the catalyst surface at state i, and P_i is the probability of the system being in state i. The change of the average number of A adsorbed on the surface can therefore be expressed as

$$\frac{\mathrm{d}\langle A\rangle}{\mathrm{d}t} = \sum_i \frac{\mathrm{d}P_i}{\mathrm{d}t}A_i = \sum_i \left(\sum_j [W_{ij}P_j - W_{ji}P_i]\right)A_i = \sum_i\sum_j W_{ij}P_j(A_i - A_j). \tag{3.3}$$

For diffusion processes, the number of A adsorbed on the catalyst surface before and after the event is constant, and therefore, the time derivative is zero. However, for a specific reaction $\mathrm{A}+\mathrm{B} \longrightarrow \mathrm{AB}$, the number of A adsorbed on the surface decreases. In this case $A_i - A_j = -1$. If adsorbate-adsorbate interaction are neglected, and all surface sites have identical chemical properties, the transition rate is the same for all events transferring A and B to AB, namely the rate constant, k. From each configuration j, $(AB)_j^{\mathrm{pair}}$ number of final states i can be obtained, where $(AB)_j^{\mathrm{pair}}$ is the number of AB-pairs in state j. With this approach, the change of the number of A adsorbed on the surface is expressed as

$$\frac{\mathrm{d}\langle A\rangle}{\mathrm{d}t} = \sum_i\sum_j W_{ij}P_j(A_i - A_j) = -k\sum_j P_j(AB)_j = -k\langle(AB)^{\mathrm{pair}}\rangle. \tag{3.4}$$

Determining the number of AB-pairs is difficult. However, the mean-field approximation offers a simple solution to this problem. In the mean-field approximation,

the adsorbates are assumed to be randomly distributed over an infinitely large catalyst surface [33]. In this case,

$$\langle (AB)^{\text{pair}} \rangle = \langle A \frac{Z}{S-1} B \rangle = \frac{Z}{S-1} (\langle A \rangle \langle B \rangle \langle (A - \langle A \rangle)(B - \langle B \rangle) \rangle) \xrightarrow{S \to \infty} \frac{Z}{S} \langle A \rangle \langle B \rangle, \tag{3.5}$$

where Z is the coordination number of each surface site, *i.e.*, the number of different ways B could be paired with A on the surface, and S is the number of surface sites. The number of surface species adsorbed on a catalyst is normally expressed with respect to the number of surface sites, resulting in the coverage, θ. Consequently, the time derivative of the coverage of A, θ_A, in the reaction between A and B can, in the mean-field approximation, be expressed as

$$\frac{\mathrm{d}\theta_A}{\mathrm{d}t} = -Zk\theta_A\theta_B. \tag{3.6}$$

This expression is, of course, only with respect to a single elementary reaction. However, it can be extended to incorporate all elementary reaction among all surface species. The general expression for the change of any coverage, with respect to any elementary reaction is

$$\frac{\mathrm{d}\theta_X}{\mathrm{d}t} = \sum_i I_i^X Z_i^* k_i f_i(\theta), \tag{3.7}$$

where I_j^X represents how many X that is formed or consumed in reaction i, Z_i^* is the coordination number for the surface of interest, k_i is the rate constant of the elementary reaction i and f_i is a function of all coverages involved in the elementary reaction. It should be noted that Z_i^* is 1 if the specific elementary reaction require only one surface site, as in certain adsorption and desorption events. For adsorption and desorption processes of a molecule A, where only one surface site is involved, the change in coverage due to the two events are

$$\frac{\mathrm{d}\theta_A}{\mathrm{d}t} = k_{\text{ads}}\theta_* - k_{\text{des}}\theta_A, \tag{3.8}$$

where θ_* is the fraction of empty surface sites. If A is the only specie on the catalyst surface $\theta_* = 1 - \theta_A$. The time derivative of all coverages form a closed set of coupled differential equations, that must be solved to obtain the time evolution of the different coverages. The mean-field approximation is an exact solution if the surface is infinitely large, all surface sites are identical, and no adsorbate-adsorbate interactions are present. However, to describe kinetic reactions over nanoparticles, with a multitude of different active sites, and also include adsorption-adsorption interactions, other methods must be employed. One of these methods is kinetic Monte Carlo (kMC) simulations, in which the chemical master equation is solved numerically, in a stochastic way, to obtain information of the time-evolution of the catalytic reaction.

3.2 Kinetic Monte Carlo Modeling

Kinetic Monte Carlo simulations are a numerical approach to solve for the time-evolution of a catalytic reaction, in accordance with the chemical master equation. Numerous kinetic Monte Carlo methods exist in literature, *e.g.* the variable step size method, the random selection method, and the first reaction method [33]. In this work, a nearest-neighbor approach using the first reaction method has been employed to investigate the catalytic reactions. The approach is as follows:

1. The system is initialised. The surface sites are initialised according to the structure of interest, *e.g.*, an extended (111) surface, or a nanoparticle of chosen size and shape. The time t is set to an initial time, and the reaction conditions, such as temperature, gas pressures and initial coverages, are set. The neighbours of each surface site are listed, to know whether species on the surface are close enough for specific elementary reactions to take place. For each surface site or pair of neighbouring surface sites, all possible events are listed. Each event is assigned a time of occurrence, according to

$$t_{\text{occurrence}} = t - \frac{1}{k}\ln(u), \tag{3.9}$$

where k is the rate constant of the event, and u is a uniform random number in the interval (0,1].

2. The system is updated according to the event with the lowest time of occurrence among all possible events, *i.e.*,

$$t_{\text{new}} = t_{\text{old}} + t_{\text{occurrence}}^{\text{min}}. \tag{3.10}$$

The elementary reactions that are no longer possible after the update of the system are removed from the list, whereas newly enabled events are added to the list, with their respective time of occurrences. Rate constants for previously possible events that are still possible, that might be affected by the surrounding species, are updated, and new time of occurrences are calculated. The reaction conditions, together with the rate constants, can in this step also be updated, if specific events have occurred, or if the time reaches a certain point. The positions of the surface sites can, in principle, also be updated in this step. However, for reactions that occur at two sites, it is also essential to update the neighbours of the affected surface sites. Important statistics are saved, such as executed events and the coverage of each surface site.

3. The time-evolution of the system is stopped if the specific reaction time is

met, or enough statistics have been collected.

The Monte Carlo approach when assigning the time of occurrences is important, so that the configuration space along the events with the largest rate constants are not sampled all the time. According to the chemical master equation, if N reaction events $R_1, R_2, ..., R_N$ are possible at a specific time with the corresponding rate constants $k_1, k_2, ..., k_N$, the system must be updated according to R_j with probability

$$p(R_j) = \frac{k_j}{\sum_{i=1}^{N} k_i}. \tag{3.11}$$

It is not obvious that the method to update the system in the first reaction method obeys this criteria. The time of occurrence for any event, with respect to the time of the simulation, is given by

$$t = -\frac{1}{k}\ln(u) \iff t = -\frac{1}{k}\ln(1-u) = F(u). \tag{3.12}$$

The probability distribution of t can be obtained from

$$p(t) = \frac{\mathrm{d}}{\mathrm{d}t}F^{-1}(t) = \frac{\mathrm{d}}{\mathrm{d}t}(1-\mathrm{e}^{-kt}) = k\mathrm{e}^{-kt}, \tag{3.13}$$

where F^{-1} is the inverse function of F. The criteria that the system is updated according to reaction R_j is that the time of occurrence is the shortest for reaction j, *i.e.*, $t_j < t_1, ..., t_{j-1}, t_{j+1}, ..., t_N$. The probability of reaction R_j being executed is therefore given by

$$p(R_j) = \int_0^\infty \mathrm{d}t_j k_j \mathrm{e}^{-k_j t_j} \int_{t_j}^\infty \mathrm{d}t_1 k_1 \mathrm{e}^{-k_1 t_1} \cdots \int_{t_j}^\infty \mathrm{d}t_N k_N \mathrm{e}^{-k_N t_N} \tag{3.14}$$

$$= \int_0^\infty \mathrm{d}t_j k_j \mathrm{e}^{-k_j t_j} \mathrm{e}^{-k_1 t_j} \cdots \mathrm{e}^{-k_N t_j} = \int_0^\infty \mathrm{d}t_j k_j \mathrm{e}^{-t_j \sum_i k_i} \tag{3.15}$$

$$= \frac{k_j}{\sum_{i=1}^{N} k_i}, \tag{3.16}$$

which is consistent with the chemical master equation.

3.3 Comparison between Mean-field and kMC Modeling

In the most basic case, when the reaction consists of only adsorption and desorption of a single specie A, occupying one surface site, and adsorbate-adsorbate

interactions are neglected, it is easy to compare the results obtained from the kinetic Monte Carlo simulations with the analytical solution of the coverage. The coverage of A as a function of time, is given from the mean-field approximation as:

$$\frac{\mathrm{d}\theta_A(t)}{\mathrm{d}t} = k_{\mathrm{ads}}(1-\theta_A(t)) - k_{\mathrm{des}}\theta_A(t) \implies \theta_A(t) = \frac{k_{\mathrm{ads}}}{k_{\mathrm{ads}}+k_{\mathrm{des}}}\left(1-\mathrm{e}^{-(k_{\mathrm{ads}}+k_{\mathrm{des}})t}\right). \tag{3.17}$$

In Figure 3.2, the coverages obtained from the analytical solution and the kinetic Monte Carlo simulations over a (20, 20) surface grid, for different ratios between the adsorption rate constant and desorption rate constant, are presented. The red, black and blue curves are the results obtained from the ratios 4, 1, 1/4, respectively. In the analytical solution, the coverages converge toward 0.8, 0.5 and 0.2, respectively. At these coverages the adsorption rate and desorption rate are equal, since the ratio between empty sites and covered sites are equal to the ratio between the rate constants. For the kinetic Monte Carlo simulations, the same average coverage is obtained. However, due to the finite site of the grid, fluctuations around the mean value will occur. This behaviour is consistent with experimental measurements, since real systems are not infinitely large, as is assumed in the mean-field approximation. However, even though more accurate results can be obtained from kinetic Monte Carlo simulations as compared to mean-field simulations, the analysis of the results are more challenging.

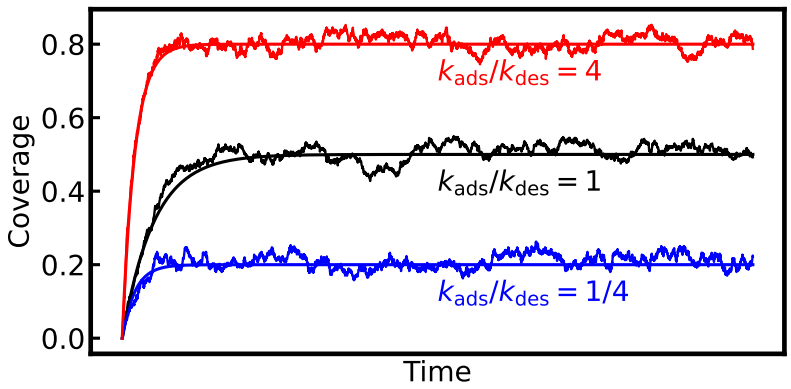

Figure 3.2: The coverage as a function of time, obtained from the mean-field approximation and kinetic Monte Carlo simulations, for different ratios between the adsorption and desorption rate constants.

3.4 Analysis of Reaction Kinetics

An optimal catalyst has the highest possible reaction rates towards the desired products, whereas the reaction rates towards undesired products are low. The formation rate of products in a catalytic reaction is often expressed as a turn-over frequency (TOF). The TOF is defined as the number of molecules formed per catalytic site and second. The molecules may be the desired product, or undesired products formed over the catalyst, and the TOF can, therefore, be defined for each product. A high TOF towards the desired product corresponds to a high reaction rate. However, it is also important that the catalyst promotes the formation of desired products, as compared to undesired products. A measure of how well the catalyst steers the reaction towards the desired products is the selectivity, S, defined as:

$$S = \frac{\sum_i \mathrm{TOF}_i^{\mathrm{desired}}}{\sum_i \mathrm{TOF}_i^{\mathrm{desired}} + \sum_j \mathrm{TOF}_j^{\mathrm{undesired}}}. \tag{3.18}$$

It can be difficult to find a catalyst with both a high TOF and high selectivity towards the desired products. Whether a high TOF or a high selectivity is most important depends on the reaction of interest. In reactions developed to rapidly reduce the amount of hazardous molecules from *e.g.*, combustion engines, a high TOF is important. However, in reactions where expensive reactants are used, the selectivity is crucial.

The TOF and selectivity of a reaction over a catalyst surface depend on the reaction conditions under which the reaction is occurring. In heterogeneous catalysis, the reaction conditions can vary from high pressures and temperatures, with all reacting species in gas phase, to low temperatures, where the reactants and products are solvated in *e.g.* a water solution [4]. According to transition state theory, the elementary reaction rates scale exponentially with temperature. To determine the temperature dependence of the overall reaction however, an apparent activation energy E_{app} is invoked, such that the overall reaction rate, towards any product, p, can be expressed as

$$r_p = \nu \mathrm{e}^{-E_{\mathrm{app},p}/k_{\mathrm{B}}T} \prod_i [A_i]^{n_{i,p}}, \tag{3.19}$$

where the pre-exponential factor ν is assigned no temperature dependence. Note that the apparent activation energy is, therefore, not the same as the activation energy, since ν is, *de facto*, temperature dependent, see 2.2. The apparent activation energy towards any product is defined as

$$E_{\mathrm{app},p} = k_{\mathrm{B}}T^2 \frac{\partial \ln(r_p^+)}{\partial T}, \tag{3.20}$$

where r_p^+ is the forward reaction rate towards product p, *i.e.*, the TOF of p if no reverse reactions are occurring. The apparent activation energy is often temperature dependent, and difficult to extrapolate to other temperatures. The dependence on the activity $[A_i]$ of the reacting species *e.g.*, pressures and concentrations, on the overall reaction rate towards any product, p, is given by the reaction order $n_{i,p}$. The reaction orders are calculated as

$$n_{i,p} = [A_i] \frac{\partial \ln(r_p^+)}{\partial [A_i]}. \tag{3.21}$$

The apparent activation energies and reaction orders can be measured experimentally. Therefore, experimental results are often used to determine the accuracy of the kinetic models. By analysing the apparent activation energies and reaction orders, it is possible to optimize the reaction conditions for a catalytic reaction, with respect to the TOF, and the selectivity towards the desired products. This can, in principle, be done either by computational approaches or experimental observations. However, to explain the reaction mechanism and find kinetic bottlenecks, kinetic models are crucial.

4

Modeling Reactions over Nanoparticles

The potential energy surface along the reaction coordinate is often represented with an energy diagram. An example of an energy diagram for the reaction $A_2 + B_2 \longrightarrow A_2B_2$ for a specific catalytic site is shown in Figure 4.1. In the energy diagram, * denotes an empty surface site, whereas *e.g.*, $B_2{}^*$ denotes B_2 adsorbed on the catalyst surface. The blue path represents the energies along the path forming the desired product A_2B_2, while the red path represents the path towards the undesired product AB_2. The formation of A_2B_2 contains a series of elementary reactions. Firstly, B_2 is adsorbed and dissociated on the surface, whereafter A_2 is adsorbed. Dissociated B reacts with A_2 twice, to form A_2B_2, which desorbs. The undesired product AB_2 can form in multiple positions along the reaction coordinate forming A_2B_2. The side reactions compete with the formation of the desired product. The selectivity depends on the rates towards the desired products and the undesired products. Since the rate of an elementary reaction depends on both the energy barrier, and the coverages on the surface, it is not trivial to determine the selectivity directly from the energy diagram. It should be noticed that in a deficit of adsorbed B on the surface, the side reactions may have higher rates, despite the rate constants being lower than along the path forming A_2B_2. In this chapter, methods to describe the kinetics over particles with a large number of different catalytic sites are discussed. A few key results from the papers are discussed, including site-communication in the direct formation of H_2O_2 over dilute PdAu nanoparticles and the effects of the metal-water interface and the dynamics of dilute PdAu alloys.

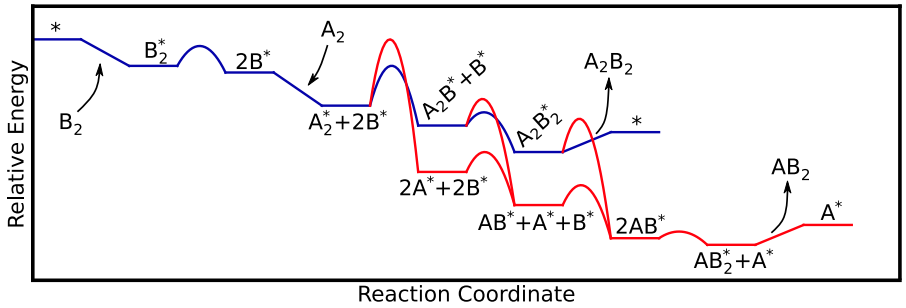

Figure 4.1: An energy diagram along the reaction coordinate for the reaction $A_2 + B_2 \longrightarrow A_2B_2$. The blue path represents the reaction towards the desired product A_2B_2, whereas the red path represents the formation of the undesired product AB_2.

4.1 Scaling Relations

The energy diagram shown in Figure 4.1 depends on the active site, on which the reaction occurs. On other catalytic sites, with different chemical properties, the energy diagram may be altered [73–77]. Real catalysts contain a large number of different sites. In figure 4.2, two possible catalyst surfaces are shown. The surface atoms are color coded according to the coordination number *i.e.*, the number of nearest neighbors. Dark grey, light grey, yellow, red, green and blue colors correspond to coordination numbers of 10, 9, 8, 7, 6, and 3, respectively. In Figure 4.2a, a (111) surface with a step is visualized. The surface step contains a vacancy, and an ad-atom is placed on the (111) surface. In Figure 4.2b, a truncated octahedron nanoparticle is visualized. An atom located on the corner of the nanoparticle has been removed from the original position to form an ad-atom on a (111) facet. Species adsorbed on the surfaces shown in Figure 4.2, can adsorb on top of a single atom (atop sites), over two atoms (bridge sites), or between 3 or 4 atoms in the surface (hollow sites). This leads to a large number of possible structural configurations. The adsorption energies and transition state energies over all possible sites are difficult to calculate explicitly. A way to ease the computational difficulty in obtaining the energy diagram for each site explicitly, is to use scaling relations.

4.1.1 Descriptors

One type of scaling relation is the prediction of adsorption energies, using a descriptor [76, 78, 79]. The coordination number of an atom is one type of descriptor. A more extensive descriptor, that has shown to provide good predictions of the

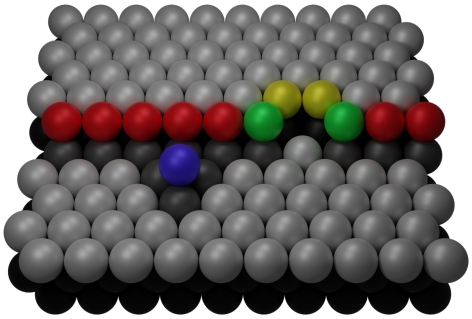

(a) A (111) surface with a step and a defect in the form of an ad-atom, stemming for the step.

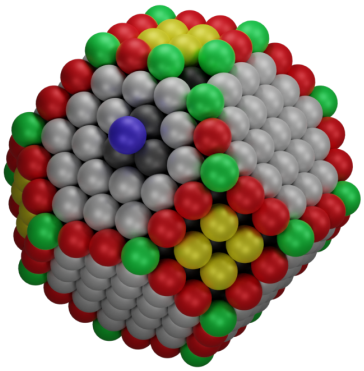

(b) A truncated octahedron nanoparticle with a defect in the form of an ad-atom, stemming from the corner of the nanoparticle.

Figure 4.2: Atomic models of two possible catalysts. In (a) a stepped (111) surface with a defect is shown. In (b) a truncated octahedron nanoparticle with a defect is visualized. The atoms are color coded according to the coordination number. Color codes: CN=10 (dark grey), CN=9 (light grey), CN=8 (yellow), CN=7 (red), CN=6 (green) and CN=3 (blue).

adsorption energies over both Au and Pt, is the generalized coordination number [79, 80]. The generalized coordination number also takes next-nearest neighbors into account, and is defined as

$$\mathrm{GCN} = \frac{1}{\mathrm{CN}_{\mathrm{max}}} \sum_i \mathrm{CN}_i, \tag{4.1}$$

where the summation is taken over all nearest neighbors of the surface site and $\mathrm{CN}_{\mathrm{max}}$ is the maximum CN for the specific adsorption site in the bulk structure. Finding a descriptor to describe the energies of the transition state on different sites is more challenging. It is commonly done using the Brønstedt-Evans-Polanyi relation, in which the transition state energy of an elementary reaction is estimated as a linear combination of the energies of the initial and final state configurations [81]. With this approach, the elementary reaction energy, obtained from the descriptor, can be used to also calculate the elementary reaction barrier.

In practice, the scaling relations are obtained from explicit calculations over a range of model surfaces. From the adsorption energies and transition state energies, a suitable descriptor is chosen, and a regression is performed. The functions can thereafter be used to predict the adsorption and transition state energies for other catalytic sites, with different value of the descriptor. A visualization of the scaling relations are shown in Figure 4.3. In the figure to the left, a linear relation between

the descriptor and the explicitly calculated adsorption energies, for two different adsorbates, are shown. In the figure to the right, the Brønstedt-Evans-Polanyi relation between the the adsorption energies and the transition state energies are visualized.

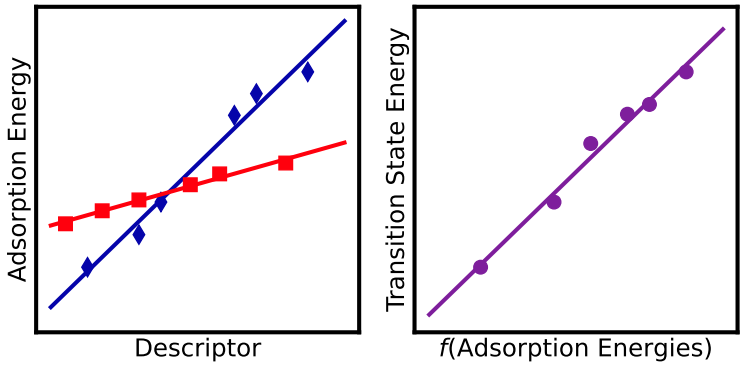

Figure 4.3: A visualization of scaling relations, used to predict the adsorption energy from a descriptor (left), and the transition state energy for a specific elementary reaction from the initial and final state adsorption energies (right).

4.2 Kinetic Coupling

The presence of a variety of different active sites on a catalyst surface can sometimes have important consequences for the reaction mechanism and the efficiency of the catalyst [38, 82]. In Figure 4.4, the potential energy diagrams for a reaction constituted by two elementary reactions, are shown. In the energy diagram to the left, both elementary reactions occur on site A. The first process has a low barrier, whereas the activation energy for the second elementary reaction is high. The turn-over frequency at 100 °C is only 4.8×10^{-4}/s, with an apparent activation energy of 1.23 eV. The situation is different over site B (middle energy diagram), where the barrier for the first elementary reaction is high, and the second barrier is low. Over site B, the turn-over frequency is 5.4/s and the apparent activation energy is 0.93 eV at 100°C. Regardless of whether the reaction occurs solely on site A or solely on site B, the TOF is truncated by one of the barriers. However, if the elementary reactions can occur on both sites, the situation is different. In this case, the first elementary reaction occurs on site A. The intermediate specie may diffuse to site B, on which the second elementary reaction can occur. In this case, the reaction can proceed without any of the high barriers. The TOF and activation energy are in these cases 2700/s and 0.73 eV at 100°C, respectively. It should be

noticed that the kinetic coupling can accelerate the formation of both desired and undesired products, hence possibly lowering the selectivity.

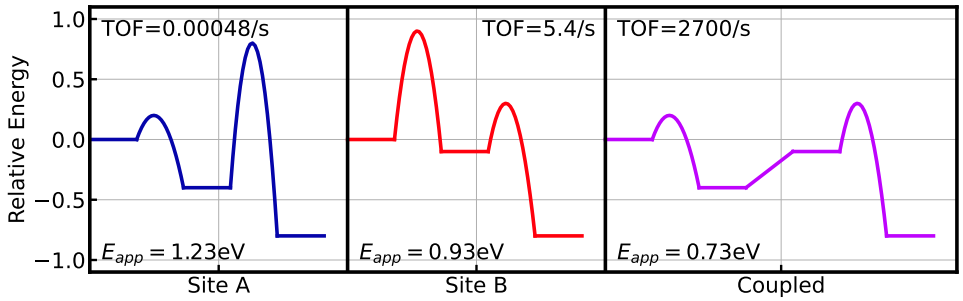

Figure 4.4: Energy diagrams for a reaction constituted of two elementary reactions. In the energy diagram to the left, the reaction occurs solely on site A, whereas in the middle diagram, both elementary reactions occur on site B. In the energy diagram to the right, the elementary reactions can occur on either site. For each energy diagram, the TOF and apparent activation energy at 100°C are presented.

4.3 Breaking the Scaling Relations with Alloys

Even with kinetic coupling between different active sites, a high TOF and selectivity are sometimes difficult to obtain over mono-metallic catalysts [42, 83]. Owing to the linear behavior of the potential energy surface with respect to certain descriptors, large differences in energy diagrams, such as in 4.4, are difficult to obtain over mono-metallic particles. One way to overcome this problem is by mixing two different metals, forming an alloy [42, 83, 84]. The dilute limit, where single monomers are embedded in another metal host, are known as single-atom-alloy (SAA) catalysts. SAA catalysts have shown to be more efficient than their mono-metallic counterparts in a range of reactions, including partial hydrogenation of hydrocarbons over dilute PdCu [38, 85], hydrogenation of propenal over dilute PdAg [86] and direct H_2O_2 formation from H_2 and O_2 over dilute PdAu [54]. The reason for the improved selectivity has been assigned to the suppression of active sites [42], geometric effects [54], and the site communication between different active sites [87].

4.4 Direct Formation of H_2O_2

In the case of direct H_2O_2 formation from H_2 and O_2 over dilute PdAu particles in an aqueous solution, the kinetic coupling is pivotal for the high selectivity. Over

pure Pd nanoparticles, the selectivity towards H_2O_2 is low, due to irreversible O–O bond rupture [44]. Over pure Au nanoparticles, the TOF of H_2O_2 is low [51], since H_2 can not dissociate on the surface. However, with SAAs of Pd embedded in Au nanoparticles in an aqueous solution, the turn-over frequency is significantly increased, and the selectivity is close to 100 %. In **Paper I**, kinetic Monte Carlo simulations reveal that H_2 adsorbs and dissociates on the Pd monomers, whereas the reduction of oxygen occurs on the under-coordinated Au atoms, located at the edges and corners of the nanoparticles. The site separation of the different elementary reactions is in this reaction crucial for the selectivity, since the selectivity on under-coordinated Pd monomers is low. In Figure 4.5, four different SAA nanoparticles are visualized. The selectivity towards H_2O_2 is high at 1 bar O_2 and H_2 pressure at 286 K, regardless of whether one or eight Pd monomers are placed in the (111) facets. However, under-coordinated Pd monomers on the nanoparticle edges irreversibly form H_2O. Therefore, the selectivity is decreased when the number of under-coordinated Pd monomers increases from one to eight, since more oxygen reduction occurs on Pd instead of the Au edges and corners. However, selectivities approaching 100 % can be obtained, also over ill-compositioned nanoparticles, at increased H_2 pressures. In this case, the site separation between H_2 dissociation and oxygen reduction is emphasised, as the Pd monomers are covered by H.

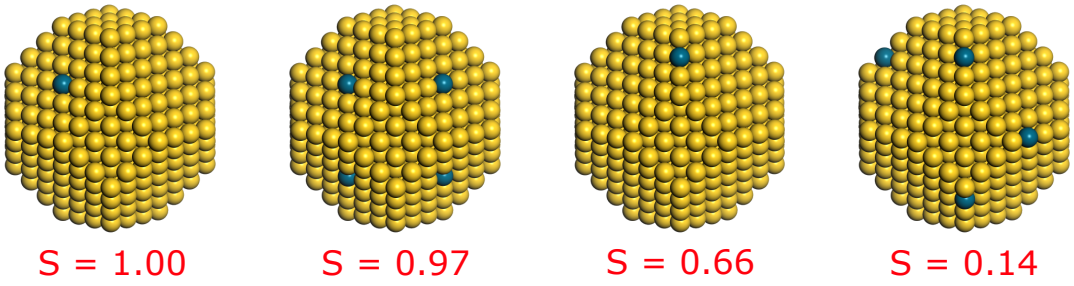

Figure 4.5: Au nanoparticles with 1) 1 Pd monomer embedded in a (111) facet, 2) 8 Pd monomers embedded in different (111) facets, 3) 1 Pd monomer embedded in an edge, and 4) 8 Pd monomers embedded in different edges. The selectivity towards H_2O_2 at 1 bar H_2 pressure and 1 bar O_2 pressure at 286 K, for each nanoparticle composition is presented.

4.5 Reactions at Solid-Liquid Interfaces

Many catalytic reactions required in sustainable energy applications occur at the interface between a catalyst and a liquid solvent [88–90]. A liquid solvent can affect the catalytic reaction in several ways, altering the potential energy landscape, and

consequently shift the TOF and selectivity of the reaction [53, 91–94]. The effects can stem from stabilization of certain intermediates on the surface, due to *e.g.*, hydrogen bonds, or altered adsorption and desorption rates. However, a solution may have more direct implications on the catalytic reaction than only shifting the rates of elementary reactions. H_2O and CH_3OH molecules adsorbed on the surface could act as a bridge between surface bound hydrogen and reaction intermediates, hence cocatalysing the reaction [54, 94]. Another possibility is the complete charge separation of surface bound hydrogen, in which a proton is donated to the water solution, whereas the electron is left in the metal surface [48, 95]. In **Paper I**, it is shown that complete charge separation of hydrogen adsorbed on Au or on Pd monomers embedded in Au is strongly exothermic and accompanied by low barriers. A visualization of the complete charge separation is shown in Figure 4.6. In the initial state, hydrogen is adsorbed on the metal surface. The transition state is reached when H reaches an atop position, directly under a water molecule. The final state configuration shows the water solvated proton, in the form of H_3O^+ over a negatively charged metal surface.

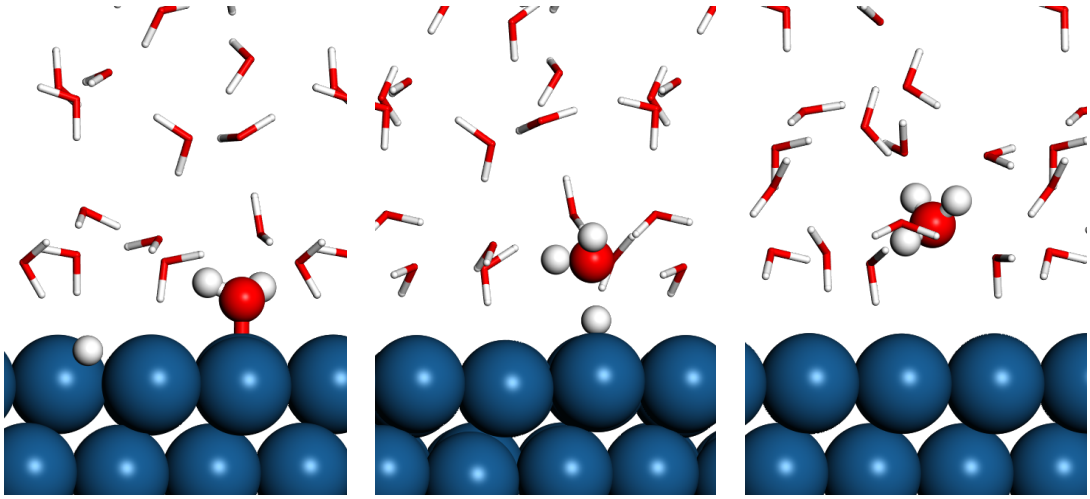

Figure 4.6: Atomic models of the charge separation process over Pt(111). In the model to the left, H is adsorbed on the metal surface under a water layer. In the middle model, H has diffused to an atop position, directly under a water molecule. In the right figure, the charge separated state is shown, where a proton is solvated in the water solution, over a negatively charged surface. Atomic color codes: Pt (blue), O (red), and H (white).

The spontaneous charge separation of H, forming a water solvated proton over a negatively charged metal surface, has important implications in the direct formation of H_2O_2, as the recution of oxygen can occur via the water solution, instead of

in conventional surface reactions. A visualization of the consequences is shown in Figure 4.7. Since the reduction of oxygen is competing with the irreversible O–O bond rupture, the height of the energy barriers in the addition of hydrogen to the oxygen species are crucial for the selectivity.

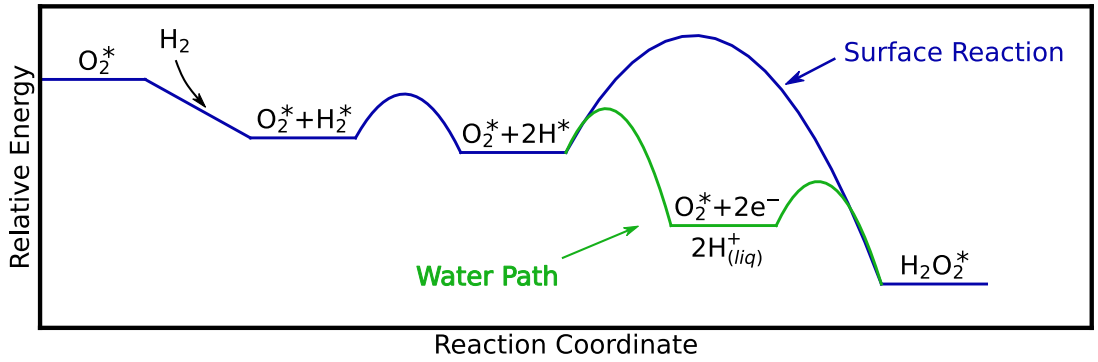

Figure 4.7: An energy diagram, visualizing the importance of the charge separation process in the direct formation of H_2O_2. The reactions between hydrogen and the oxygen species on the surface are associated with high barriers. However, reactions via the water solution increases the formation rate of H_2O_2.

In **Paper II**, the influence of the metal-water interface is investigated in detail for the (111) surfaces of Cu, Ag, Au, Pd, and Pt. Constrained molecular dynamics simulations, in combination with the blue-moon ensemble method, are employed to investigate the electronic and free energy profiles of the complete charge separation process. The simulations show that complete charge separation is exothermic over Au, Ag, and Pt, whereas it is close to thermo-neutral over Pd, and endothermic over Cu. The energy barriers upon charge separation over Au and Pt are only 0.3 eV and 0.4 eV, respectively. Thus, charge separation is facile at room-temperature. Furthermore, the free energy barriers are similar to the electronic energy barriers, implying that the entropy contributions in the process are small.

The calculations in **Paper II** show that the presence of water affects also the adsorption properties of O_2. The adsorption strength of O_2 on Au(111), Pt(111) and Pd(111) is increased by 0.2–0.3 eV, as compared to the adsorption in the absence of water. The effects are larger on Ag(111), where the adsorption energy of O_2 increases $\sim$1 eV in the presence of water. The increased adsorption strength over the different surfaces stems from hydrogen bonds between adsorbed O_2 and the water molecules in the solution. The hydrogen bonds promote a significant charge transfer from the metal surface, to the adsorbed O_2 molecule, substantially elongating the O–O bond.

4.6 Dynamics of Nanoparticles

In **Paper I**, it is shown that the turn-over frequency and selectivity towards H_2O_2 depends on the location of the Pd monomers. In an inert atmosphere, the more active metal monomers are, in most cases, preferably located in the subsurface layers of the nanoparticle [85]. However, previous calculations and experimental results have shown that in a CO atmosphere, the active monomers are stabilized on the surface [96, 97].

Investigating the kinetics of the activation of SAA nanoparticles is important, as the dynamics of the particles may be kinetically limited. Since the active state of a SAA nanoparticle is a meta-stable configuration, rather than the thermodynamically most stable configurations, the kinetic understanding is important to describe the durability of the catalyst. In **Paper III**, the kinetics of the activation and deactivation of PdAu SAA nanoparticles are investigated, using kinetic Monte Carlo simulations. The potential energy surface reveals that CO stabilizes Pd monomers in the Au surface. However, a CO pressure also facilitates the formation of vacancies in the nanoparticle, crucial for the diffusion of Pd. In the vacancy formation process, an Au atom on the surface is moved to an fcc-hollow site on the surface, forming an ad-atom. In Figure 4.8, the coverage of ad-atoms on three model systems are presented. The model systems are a 20x20 (111) surface, constituted of 10 atomic layers (red), a 20x20 (111) surface with two (211) steps, constituted of 10 atomic layers (orange), and a 3.6 nm truncated octahedron nanoparticle (green). In the absence of CO, the coverage of ad-atoms on the (111) surface is low. However, when steps are introduced on the surface, the ad-atom coverage significantly increases. The ad-atom coverage is further increased over the nanoparticle. The reason for the increased coverage is the lower activation energy associated with vacancy formation of under-coordinated Au atoms. When a CO pressure of 1 bar is introduced to the systems, the ad-atom coverages are notably increased. Adsorbed CO molecules facilitate the formation of vacancies by stabilizing the transition state, as well as the ad-atom on the surface. This effect is most notable over the (111) surface, on which the CO adsorption energy is low. The deactivation of the SAA catalysts, *i.e.*, the diffusion of Pd monomers from the surface to the subsurface layers, are found to depend on both the position of the Pd monomers, and the global structure of the catalyst. In an inert atmosphere, the lifetime of Pd embedded in a (111) surface is long at 373 K, despite being a meta-stable composition of the catalyst. However, if the Pd monomer is instead located in a (111) facet of a nanoparticle, the catalyst is deactivated after $\sim$1 hour. Importantly, the Pd monomers located at under-coordinated positions are not stable for more than a couple of minutes. This emphasises the importance of taking both the local environment, and the global structure of the catalyst into account

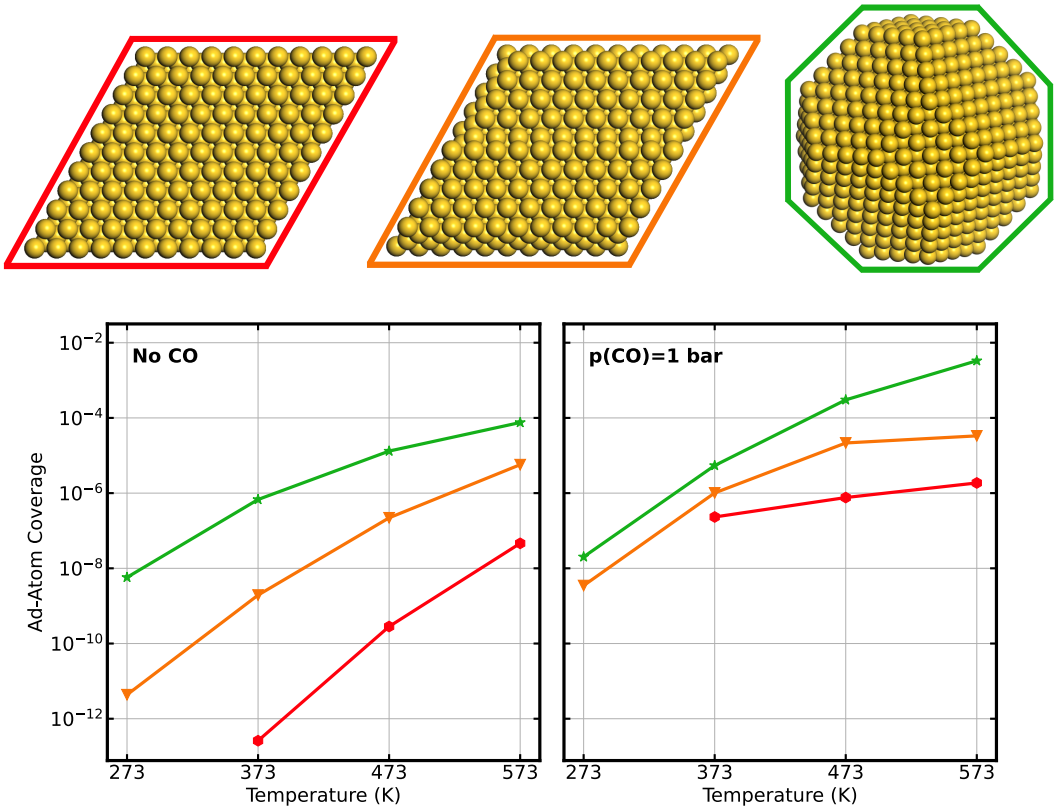

Figure 4.8: The coverage of ad-atoms on Au(111), Au(111) with two steps, and a 3.6 nm truncated octahedron nanoparticle, as a function of temperature. In the figure to the left, the ad-atom coverages in an inert atmosphere are presented. In the figure to the right, the ad-atom coverages at 1 bar CO pressure are presented.

when investigating the composition and dynamics of SAA catalysts.

5

Conclusions

In this thesis, the kinetics of catalytic reactions is explored using first-principles based kinetic Monte Carlo simulations. Density functional theory calculations are applied to determine the adsorption energies and elementary reaction rates over a range of model systems. To describe the potential energy landscape over nanoparticles, scaling relations, based on the coordination of the catalytic sites, are used. To explore the potential energy surface in the case of many close-lying minima, constrained molecular dynamics simulations are used.

Specifically, the direct synthesis of H_2O_2 from H_2 and O_2 over dilute PdAu nanoparticles in an aqueous solution is investigated. The reaction depends on Pd being located in the surface of the catalyst. Therefore, kinetic Monte Carlo simulations are employed to investigate the dynamics of nanoparticles in an inert atmosphere, and in a CO atmosphere. Specifically, the activation, in the presence of CO, and the deactivation, in the absence of CO, of the dilute PdAu alloys are studied. Apart from stabilizing the Pd monomers in the Au surface, CO is found to also facilitate the formation of vacancies in the system, which is crucial for the segregation of Pd. The vacancies are preferably formed on the edges and corners of the nanoparticle, but may diffuse both in the surface and in the subsurface of the nanoparticles. The deactivation of the particles, in the absence of CO is dependent both on the location of the Pd monomer and the global structure of the system. The deactivation is slow at temperatures below 373 K, suggesting that the dilute PdAu nanoparticles reside in meta-stable configuration during reactions.

The kinetics of the direct formation of H_2O_2 over different PdAu systems are explored using scaling relation kinetic Monte Carlo simulations. Whereas low amounts of H_2O_2 is formed over pure Au nanoparticles, and pure Pd nanopar-

ticles suffer from low selectivity towards H_2O_2, the dilute PdAu nanoparticles are shown to be both active and highly selective towards H_2O_2. The selectivity is found to depend on the efficient separation of elementary reactions over the different active sites. The Pd monomers act as active centers for H_2 dissociation, whereas the formation of H_2O_2 occurs on the under-coordinated Au sites at the edges and corners of the nanoparticles. The site-separation is crucial for the reaction, as the selectivity towards H_2O_2 on under-coordinated Pd monomers is low. The reaction is found to occur via redox-reactions at the metal-water interface. H adsorbed on the metal surface undergoes a charge separation, in which a proton desorbs to the water layer, whereas the electron is donated to the metal surface. As the formation of H_2O_2 is competing with the irreversible rapture of $O-O$ bonds on the surface, the facile charge separation is crucial to maintain a high selectivity.

The facile charge-separation of H at the metal-water interface could be important also for other catalytic reactions. The charge-separation process was therefore investigated in detail over the (111) surfaces of Cu, Ag, Au, Pd, and Pt. The electronic and free energy profiles for the charge separation of H over the different surfaces are mapped with constrained molecular dynamics simulations. The process is found to be exothermic over Ag, Au, and Pt, close to thermo-neutral over Pd and endothermic over Cu. The process is over Au and Pt associated with low barriers, thus, being facile at room-temperature. Water is also shown to have effects on the adsorption properties of O_2. In water, the O_2 adsorption strength and $O-O$ bond length is significantly increased, as compared to the adsorption in the absence of water. The increased adsorption strength stems from the enabled hydrogen bonds between the water molecules and the adsorbed O_2, facilitating a significant metal-to-O_2 charge transfer, and an elongation of the $O-O$ bond.

5.1 Limitations

The exact description of a catalytic reaction is challenging, and the accuracy of the predictions are limited by several factors. A clear limitation is the accuracy of the density functional theory calculations, which are employed to describe the potential energy landscape. Since the rate of an elementary reaction is exponentially dependent on the activation energy, small errors in the barrier height, lead to large changes of the elementary reaction rates. For example, an activation energy shift of 0.1 eV leads to a factor 50 change in the elementary reaction rate at room-temperature. This is a problem, since the energies depend on the choice of exchange-correlation functional. Due to the large energy dependence when assigning the elementary reaction rates, the turn-over frequency of a specific reaction is difficult to obtain. However, this limitation has a smaller impact when analysing

the trends of catalytic reactions with respect to temperature, reaction conditions, or catalytic sites. A way to further increase the accuracy of catalytic predictions in the future is to use more accurate methods to calculate the energies, *e.g.*, the random phase approximation [98], or to include error estimates in the rates when modeling the catalytic reaction.

A further limitation in the modeling of kinetic reactions is the clear gap between experiments and the theoretical structural models. It is difficult to perfectly mimic the experimental conditions, as impurities and other small deviations from perfect conditions tend to be either neglected or over-estimated in kinetic models. The periodic model systems used to describe the potential energy landscape over nanoparticles are often small, and trace elements are therefore difficult to describe. In the modeling of catalytic reactions, elementary reactions are often included based on chemical intuition or previous kinetic models. However, as described in the appended papers, reaction mechanisms not following conventional surface reactions may be important. Deviations in results obtained from computational models and experiments may stem from comparing different things. In experiments, an ensemble of different nanoparticles are considered, whereas in kinetic models, the results are obtained for individual nanoparticles. It should be emphasised that the advances in catalysis are based on the interplay between experiments and computational models, and that the purpose of kinetic models is to aid the interpretation of experimental results, and to understand the mechanisms in the reactions.

5.2 Outlook

There are many things still to be explored. Kinetic Monte Carlo simulations can be employed to combine the dynamics of the nanoparticles with catalytic reactions on the surface. The description of the interplay between adsorbates and the structure of the catalyst is an interesting development of kinetic modeling. The description of the dynamics could be further improved by also taking the support of the nanoparticles into consideration.

The dynamics of other metal particles, including dilute alloys, in different atmospheres can be further investigated. However, when probing kinetics for a range of different systems, kinetic Monte Carlo simulations are complicated and computationally expensive. Therefore, it would be interesting to explore to what extent mean-field modeling could be incorporated into the kinetic Monte Carlo simulations. A combination might make it possible to obtain the mechanistic description of kinetic Monte Carlo simulation, at an accelerated rate. Investigating the limitations of mean-field modeling, and the possibility to include kinetic coupling also in

mean-field kinetic models, and compare the prediction to kinetic Monte Carlo simulations would also be an important fundamental investigation. A different kind of combination would also be interesting to explore, in which the kinetic Monte Carlo simulations are combined with molecular dynamics simulations. The molecular dynamics simulation could be used to further describe the dynamic behavior of the catalyst.

Kinetic Monte Carlo simulations are highly tunable with respect to reaction conditions, and the structure of the catalyst. Therefore, a next step to further approach the real experimental conditions could be to simulate entire reactors, and *e.g.*, consider the inclusion of promotors, ligands, or other solvents.

Acknowledgments

The research presented in this licentiate thesis was performed at the Division of Chemical Physics and the Competence Centre for Catalysis, at Chalmers University of Technology, Sweden, between August 2021 and March 2024.

The research is funded by the Swedish Research Council (2020-05191). Computational time has been granted by NAISS at NSC (Linköping), and PDC (Stockholm).

The Competence Centre for Catalysis (KCK) is hosted by Chalmers University of Technology and is financially supported by the Swedish Energy Agency and the member companies Johnson Matthey, Perstorp, Powercell, Preem, Scania CV, Umicore, and Volvo Group.

Additionally, I would like to express my gratitude to:

My supervisor, Professor Henrik Grönbeck. Thank you for being so supportive, and for sharing my enthusiasm for the research that we do. It is a privilege to learn from your expertise and understanding of physics in general, and catalysis in particular.

My co-supervisor, Professor Anders Hellman. Thank you for your formal and informal guidance.

The members of the Division of Chemical Physics, for the good working environment and the good scientific discussions.

My family. Thank you for always supporting me, and encouraging me in my interests.

Bibliography

[1] I. Chorkendorff and N. J. W., *Conceps of Modern Catalysis and Kinetics* (Wiley, 2017). ISBN 978-3-527-33268-7.

[2] M. V. Twigg, *Progress and future challenges in controlling automotive exhaust gas emissions,* Appl. Catal. B: Environ. **70**, 2 (2007).

[3] M. T. M. Koper, *Fuel cell catalysis : a surface science approach.* (Wiley, 2009). ISBN 9780470131169.

[4] R. Schlögl, *Heterogeneous Catalysis,* Angew. Chem. Int. Ed. **54**, 3465 (2015).

[5] A. J. Medford, A. Vojvodic, J. S. Hummelshøj, J. Voss, F. Abild-Pedersen, F. Studt, T. Bligaard, A. Nilsson, and J. K. Nørskov, *From the Sabatier principle to a predictive theory of transition-metal heterogeneous catalysis,* J. Catal. **328**, 36 (2015).

[6] G. Ertl, *Wilhelm Ostwald: Founder of Physical Chemistry and Nobel Laureate 1909,* Angew. Chem. Int. Ed. **48**, 6600 (2009).

[7] H. Swenson and N. P. Stadie, *Langmuir's Theory of Adsorption: A Centennial Review,* Langmuir **35**, 5409 (2019).

[8] H. Eyring, *The Activated Complex in Chemical Reactions,* J. Chem. Phys. **3**, 107 (1935).

[9] T. Nilsson Pingel, M. Jørgensen, A. B. Yankovich, H. Grönbeck, and E. Olsson, *Influence of atomic site-specific strain on catalytic activity of supported nanoparticles,* Nat. Commun. **9**, 2722 (2018).

[10] G. Binnig and H. Rohrer, *Scanning tunneling microscopy,* Surf. Sci. **126**, 236 (1983).

[11] L. Xu, K. G. Papanikolaou, B. A. Lechner, L. Je, G. A. Somorjai, M. Salmeron, and M. Mavrikakis, *Formation of active sites on transition metals through reaction-driven migration of surface atoms,* Science **380**, 70 (2023).

[12] K. Siegbahn, *Electron spectroscopy for atoms, molecules, and condensed matter,* Rev. Mod. Phys. **54**, 709 (1982).

[13] A. M. Venezia, *X-ray photoelectron spectroscopy (XPS) for catalysts characterization,* Catal. Today **77**, 359 (2003).

[14] C. M. Goodwin, P. Lömker, D. Degerman, B. Davies, M. Shipilin, F. Garcia-Martinez, S. Koroidov, J. Katja Mathiesen, R. Rameshan, G. L. Rodrigues, *et al.*, *Operando probing of the surface chemistry during the Haber–Bosch process,* Nature **625**, 282 (2024).

[15] J. W. Frenken and I. Groot, *Operando research in heterogeneous catalysis* (Springer, 2017).

[16] B. Hammer, Y. Morikawa, and J. K. Nørskov, *CO Chemisorption at Metal Surfaces and Overlayers,* Phys. Rev. Lett. **76**, 2141 (1996).

[17] M. Mavrikakis, B. Hammer, and J. K. Nørskov, *Effect of Strain on the Reactivity of Metal Surfaces,* Phys. Rev. Lett. **81**, 2819 (1998).

[18] H. Falsig, B. Hvolbæk, I. S. Kristensen, T. Jiang, T. Bligaard, C. H. Christensen, and J. K. Nørskov, *Trends in the Catalytic CO Oxidation Activity of Nanoparticles,* Angew. Chem. Int. Ed. **47**, 4835 (2008).

[19] J. K. Nørskov, T. Bligaard, J. Rossmeisl, and C. H. Christensen, *Towards the computational design of solid catalysts,* Nat. Chem. **1**, 37 (2009).

[20] A. D. Becke, *A new mixing of Hartree–Fock and local density-functional theories,* J. Chem. Phys. **98**, 1372 (1993).

[21] A. D. Becke, *Density-functional thermochemistry. I. The effect of the exchange-only gradient correction,* J. Chem. Phys. **96**, 2155 (1992).

[22] J. P. Perdew, K. Burke, and M. Ernzerhof, *Generalized gradient approximation made simple,* Phys. Rev. Lett. **77**, 3865 (1996).

[23] A. A. Gokhale, J. A. Dumesic, and M. Mavrikakis, *On the Mechanism of Low-Temperature Water Gas Shift Reaction on Copper,* J. Am. Chem. Soc. **130**, 1402 (2008).

[24] A. Trinchero, A. Hellman, and H. Grönbeck, *Methane oxidation over Pd and Pt studied by DFT and kinetic modeling,* Surf. Sci. **616**, 206 (2013).

[25] M. V. d. Bossche and H. Grönbeck, *Methane Oxidation over PdO(101) Revealed by First-Principles Kinetic Modeling,* J. Am. Chem. Soc. **137**, 12035 (2015).

[26] M. Jørgensen and H. Grönbeck, *First-Principles Microkinetic Modeling of Methane Oxidation over Pd(100) and Pd(111),* ACS Catal. **6**, 6730 (2016).

[27] L. Chen, T. V. Janssens, M. Skoglundh, and H. Grönbeck, *Interpretation of NH 3-TPD profiles from Cu-CHA using first-principles calculations,* Top. Catal. **62**, 93 (2019).

[28] M. Stamatakis and D. G. Vlachos, *Unraveling the Complexity of Catalytic Reactions via Kinetic Monte Carlo Simulation: Current Status and Frontiers,* ACS Catal. **2**, 2648 (2012).

[29] M. Pineda and M. Stamatakis, *Beyond mean-field approximations for accurate and computationally efficient models of on-lattice chemical kinetics,* J. Chem. Phys. **147**, 024105 (2017).

[30] N. Lopez, T. Janssens, B. Clausen, Y. Xu, M. Mavrikakis, T. Bligaard, and J. Nørskov, *On the origin of the catalytic activity of gold nanoparticles for low-temperature CO oxidation,* J. Catal. **223**, 232 (2004).

[31] F. Calle-Vallejo, *The ABC of Generalized Coordination Numbers and Their Use as a Descriptor in Electrocatalysis,* Adv. Sci. **10**2207644 ().

[32] B. Temel, H. Meskine, K. Reuter, M. Scheffler, and H. Metiu, *Does phenomenological kinetics provide an adequate description of heterogeneous catalytic reactions?,* J. Chem. Phys. **126**, 204711 (2007).

[33] A. Jansen, *An Introduction to Kinetic Monte Carlo Simulations of Surface Reactions.* (Springer Berlin Heidelberg, 2012). ISBN 9783642294884.

[34] M. Pineda and M. Stamatakis, *Kinetic Monte Carlo simulations for heterogeneous catalysis: Fundamentals, current status, and challenges,* J. Chem. Phys. **156**, 120902 (2022).

[35] K. Reuter, D. Frenkel, and M. Scheffler, *The Steady State of Heterogeneous Catalysis, Studied by First-Principles Statistical Mechanics,* Phys. Rev. Lett. **93**, 116105 (2004).

[36] M. Stamatakis, Y. Chen, and D. G. Vlachos, *First-Principles-Based Kinetic Monte Carlo Simulation of the Structure Sensitivity of the Water–Gas Shift Reaction on Platinum Surfaces,* J. Phys. Chem. C **115**, 24750 (2011).

[37] S. Piccinin and M. Stamatakis, *CO Oxidation on Pd(111): A First-Principles-Based Kinetic Monte Carlo Study,* ACS Catal. **4**, 2143 (2014).

[38] M. Jørgensen and H. Grönbeck, *Selective Acetylene Hydrogenation over Single-Atom Alloy Nanoparticles by Kinetic Monte Carlo,* J. Am. Chem. Soc. **141**, 8541 (2019).

[39] M. Pera-Titus, V. García-Molina, M. A. Baños, J. Giménez, and S. Esplugas, *Degradation of chlorophenols by means of advanced oxidation processes: a general review,* Appl. Catal. B: Environ. **47**, 219 (2004).

[40] R. Hage and A. Lienke, *Applications of transition-metal catalysts to textile and wood-pulp bleaching,* Angew. Chem. Int. Ed. **45**, 206 (2006).

[41] J. M. Campos-Martin, G. Blanco-Brieva, and J. L. Fierro, *Hydrogen peroxide synthesis: an outlook beyond the anthraquinone process,* Angew. Chem. Int. Ed. **45**, 6962 (2006).

[42] J. K. Edwards, B. Solsona, E. N. N, A. F. Carley, A. A. Herzing, C. J. Kiely, and G. J. Hutchings, *Switching off hydrogen peroxide hydrogenation in the direct synthesis process,* Science **323**, 1037 (2009).

[43] D. W. Flaherty, *Direct Synthesis of H2O2 from H2 and O2 on Pd Catalysts: Current Understanding, Outstanding Questions, and Research Needs,* ACS Catal. **8**, 1520 (2018).

[44] D. P. Dissanayake and J. H. Lunsford, *The direct formation of H2O2 from H2 and O2 over colloidal palladium,* J. Catal. **214**, 113 (2003).

[45] A. Plauck, E. E. Stangland, J. A. Dumesic, and M. Mavrikakis, *Active sites and mechanisms for H2O2 decomposition over Pd catalysts,* Proc. Natl. Acad. Sci. **113**, E1973 (2016).

[46] Y.-F. Han and J. H. Lunsford, *Direct formation of H2O2 from H2 and O2 over a Pd/SiO2 catalyst: the roles of the acid and the liquid phase,* J. Catal. **230**, 313 (2005).

[47] S. Abate, R. Arrigo, M. Schuster, S. Perathoner, G. Centi, A. Villa, D. Su, and R. Schlögl, *Pd nanoparticles supported on N-doped nanocarbon for the direct synthesis of H2O2 from H2 and O2,* Catal. Today **157**, 280 (2010).

[48] N. M. Wilson and D. W. Flaherty, *Mechanism for the Direct Synthesis of H2O2 on Pd Clusters: Heterolytic Reaction Pathways at the Liquid–Solid Interface,* J. Am. Chem. Soc. **138**, 574 (2016).

[49] L. Chen, J. W. Medlin, and H. Grönbeck, *On the Reaction Mechanism of Direct H2O2 Formation over Pd Catalysts,* ACS Catal. **11**, 2735 (2021).

[50] L. Chen, P. Moura, J. W. Medlin, and H. Grönbeck, *Multiple Roles of Alkanethiolate-Ligands in Direct Formation of H2O2 over Pd Nanoparticles,* Angew. Chem. Int. Ed. **61**, e202213113 (2022).

[51] J. K. Edwards, B. E. Solsona, P. Landon, A. F. Carley, A. Herzing, C. J. Kiely, and G. J. Hutchings, *Direct synthesis of hydrogen peroxide from H2 and O2 using TiO2-supported Au–Pd catalysts,* J. Catal. **236**, 69 (2005).

[52] T. Whittaker, K. B. S. Kumar, C. Peterson, M. N. Pollock, L. C. Grabow, and B. D. Chandler, *H2 Oxidation over Supported Au Nanoparticle Catalysts: Evidence for Heterolytic H2 Activation at the Metal–Support Interface,* J. Am. Chem. Soc. **140**, 16469 (2018).

[53] A. Santos, R. J. Lewis, G. Malta, A. G. Howe, D. J. Morgan, E. Hampton, P. Gaskin, and G. J. Hutchings, *Direct synthesis of hydrogen peroxide over Au–Pd supported nanoparticles under ambient conditions,* Ind. Eng. Chem. Res. **58**, 12623 (2019).

[54] T. Ricciardulli, S. Gorthy, J. S. Adams, C. Thompson, A. M. Karim, M. Neurock, and D. W. Flaherty, *Effect of Pd coordination and isolation on the catalytic reduction of O2 to H2O2 over PdAu bimetallic nanoparticles,* J. Am. Chem. Soc. **143**, 5445 (2021).

[55] M. T. Darby, E. C. H. Sykes, A. Michaelides, and M. Stamatakis, *Carbon monoxide poisoning resistance and structural stability of single atom alloys,* Top. Catal. **61**, 428 (2018).

[56] B. I. Lundqvist, A. Hellman, and I. Zorić, *Chapter 10 Electron Transfer and Nonadiabaticity* (North-Holland, 2008).

[57] R. O. Jones and O. Gunnarsson, *The density functional formalism, its applications and prospects,* Rev. Mod. Phys. **61**, 689 (1989).

[58] P. Hohenberg and W. Kohn, *Inhomogeneous Electron Gas,* Phys. Rev. **136**, B864 (1964).

[59] W. Kohn and L. J. Sham, *Self-Consistent Equations Including Exchange and Correlation Effects,* Phys. Rev. **140**, A1133 (1965).

[60] J. Kohanoff, *Electronic structure calculations for solids and molecules : theory and computational methods.* (Cambridge Univ. Press, 2006). ISBN 9780521815918.

[61] T. Thonhauser, V. R. Cooper, S. Li, A. Puzder, P. Hyldgaard, and D. C. Langreth, *Van der Waals density functional: Self-consistent potential and the nature of the van der Waals bond,* Phys. Rev. B **76**, 125112 (2007).

[62] S. Grimme, J. Antony, S. Ehrlich, and H. Krieg, *A consistent and accurate ab initio parametrization of density functional dispersion correction (DFT-D) for the 94 elements H-Pu,* J. Chem. Phys. **132**, 154104 (2010).

[63] S. Grimme, S. Ehrlich, and L. Goerigk, *Effect of the damping function in dispersion corrected density functional theory,* J. Comput. Chem. **32**, 1456 (2011).

[64] P. E. Blöchl, *Projector augmented-wave method,* Phys. Rev. B **50**, 17953 (1994).

[65] G. Henkelman and H. Jónsson, *Improved tangent estimate in the nudged elastic band method for finding minimum energy paths and saddle points,* J. Chem. Phys. **113**, 9978 (2000).

[66] G. Henkelman, B. P. Uberuaga, and H. Jónsson, *A climbing image nudged elastic band method for finding saddle points and minimum energy paths,* J. Chem. Phys. **113**, 9901 (2000).

[67] M. P. Allen and D. J. Tildesley, *Computer simulation of liquids.* (Clarendon, 1987). ISBN 0198553757.

[68] M. Iannuzzi, A. Laio, and M. Parrinello, *Efficient Exploration of Reactive Potential Energy Surfaces Using Car-Parrinello Molecular Dynamics,* Phys. Rev. Lett. **90**, 238302 (2003).

[69] J.-P. Ryckaert, G. Ciccotti, and H. J. Berendsen, *Numerical integration of the cartesian equations of motion of a system with constraints: molecular dynamics of n-alkanes,* J. Comput. Phys. **23**, 327 (1977).

[70] M. Sprik and G. Ciccotti, *Free energy from constrained molecular dynamics,* J. Chem. Phys. **109**, 7737 (1998).

[71] A. H. Motagamwala and J. A. Dumesic, *Microkinetic Modeling: A Tool for Rational Catalyst Design,* Chem. Rev. **121**, 1049 (2021).

[72] X.-Q. Zhang and A. P. J. Jansen, *Kinetic Monte Carlo method for simulating reactions in solutions,* Phys. Rev. E **82**, 046704 (2010).

[73] J. K. Nørskov, F. Abild-Pedersen, F. Studt, and T. Bligaard, *Density functional theory in surface chemistry and catalysis,* Proc. Natl. Acad. Sci. **108**, 937 (2011).

[74] K. Honkala, A. Hellman, I. N. Remediakis, A. Logadottir, A. Carlsson, S. Dahl, C. H. Christensen, and J. K. Nørskov, *Ammonia Synthesis from First-Principles Calculations,* Science **307**, 555 (2005).

[75] M. Jørgensen and H. Grönbeck, *Scaling Relations and Kinetic Monte Carlo Simulations To Bridge the Materials Gap in Heterogeneous Catalysis,* ACS Catal. **7**, 5054 (2017).

[76] M. Andersen, S. V. Levchenko, M. Scheffler, and K. Reuter, *Beyond Scaling Relations for the Description of Catalytic Materials,* ACS Catal. **9**, 2752 (2019).

[77] M. M. Montemore and J. W. Medlin, *Scaling relations between adsorption energies for computational screening and design of catalysts,* Catal. Sci. Technol. **4**, 3748 (2014).

[78] L. T. Roling and F. Abild-Pedersen, *Structure-Sensitive Scaling Relations: Adsorption Energies from Surface Site Stability,* ChemCatChem **10**1643 ().

[79] F. Calle-Vallejo, J. I. Martínez, J. M. García-Lastra, P. Sautet, and D. Loffreda, *Fast Prediction of Adsorption Properties for Platinum Nanocatalysts with Generalized Coordination Numbers,* Angew. Chem. Int. Ed. **53**, 8316 (2014).

[80] F. Calle-Vallejo, J. Tymoczko, V. Colic, Q. H. Vu, M. D. Pohl, K. Morgenstern, D. Loffreda, P. Sautet, W. Schuhmann, and A. S. Bandarenka, *Finding optimal surface sites on heterogeneous catalysts by counting nearest neighbors,* Science **350**, 185 (2015).

[81] T. Bligaard, J. Nørskov, S. Dahl, J. Matthiesen, C. Christensen, and J. Sehested, *The Brønsted–Evans–Polanyi relation and the volcano curve in heterogeneous catalysis,* J. Catal. **224**, 206 (2004).

[82] C. Vogt and B. M. Weckhuysen, *The concept of active site in heterogeneous catalysis,* Nat. Rev. Chem. **6**, 89 (2022).

[83] J. Greeley, I. Stephens, A. Bondarenko, T. P. Johansson, H. A. Hansen, T. Jaramillo, J. Rossmeisl, I. Chorkendorff, and J. K. Nørskov, *Alloys of platinum and early transition metals as oxygen reduction electrocatalysts,* Nat. Chem. **1**, 552 (2009).

[84] J. Pérez-Ramírez and N. López, *Strategies to break linear scaling relationships,* Nat. Catal. **2**, 971 (2019).

[85] R. T. Hannagan, G. Giannakakis, M. Flytzani-Stephanopoulos, and E. C. H. Sykes, *Single-Atom Alloy Catalysis,* Chem. Rev. **120**, 12044 (2020).

[86] P. Aich, H. Wei, B. Basan, A. J. Kropf, N. M. Schweitzer, C. L. Marshall, J. T. Miller, and R. Meyer, *Single-Atom Alloy Pd–Ag Catalyst for Selective Hydrogenation of Acrolein,* J. Phys. Chem. C **119**, 18140 (2015).

[87] R. Svensson and H. Grönbeck, *Site Communication in Direct Formation of H2O2 over Single-Atom Pd@Au Nanoparticles,* J. Am. Chem. Soc. **145**, 11579 (2023).

[88] N. Dubouis and A. Grimaud, *The hydrogen evolution reaction: from material to interfacial descriptors,* Chem. Sci. **10**, 9165 (2019).

[89] S. Sharma and B. G. Pollet, *Support materials for PEMFC and DMFC electrocatalysts—A review,* J. Power Sources **208**, 96 (2012).

[90] C. Samanta, *Direct synthesis of hydrogen peroxide from hydrogen and oxygen: An overview of recent developments in the process,* Appl. Catal. A **350**, 133 (2008).

[91] N. Yan, C. Xiao, and Y. Kou, *Transition metal nanoparticle catalysis in green solvents,* Coord. Chem. Rev. **254**, 1179 (2010).

[92] V. Paunovic, V. V. Ordomsky, V. L. Sushkevich, J. C. Schouten, and T. A. Nijhuis, *Direct Synthesis of Hydrogen Peroxide over Au-Pd Catalyst—The Effect of Co-Solvent Addition,* ChemCatChem **7**, 1161 (2015).

[93] P. J. Dyson and P. G. Jessop, *Solvent effects in catalysis: rational improvements of catalysts via manipulation of solvent interactions,* Catal. Sci. Technol. **6**, 3302 (2016).

[94] J. S. Adams, A. Chemburkar, P. Priyadarshini, T. Ricciardulli, Y. Lu, V. Maliekkal, A. Sampath, S. Winikoff, A. M. Karim, M. Neurock, *et al.*, *Solvent molecules form surface redox mediators in situ and cocatalyze O2 reduction on Pd,* Science **371**, 626 (2021).

[95] D. Lackey, J. Schott, J.-K. Sass, S.-I. Woo, and F. Wagner, *Surface-science simulation study of the electrochemical charge-transfer reaction (H) ad+(H2O) ad→(H3O+) ad+ e- metal on Pt (111) and Cu (110),* Chem. Phys. Lett. **184**, 277 (1991).

[96] K. G. Papanikolaou, M. T. Darby, and M. Stamatakis, *CO-Induced Aggregation and Segregation of Highly Dilute Alloys: A Density Functional Theory Study,* J. Phys. Chem. C **123**, 9128 (2019).

[97] M. Luneau, E. Guan, W. Chen, A. C. Foucher, N. Marcella, T. Shirman, D. M. Verbart, J. Aizenberg, M. Aizenberg, E. A. Stach, *et al.*, *Enhancing catalytic performance of dilute metal alloy nanomaterials,* Commun. Chem. **3**, 46 (2020).

[98] X. Ren, P. Rinke, C. Joas, and M. Scheffler, *Random-phase approximation and its applications in computational chemistry and materials science,* J. Mater. Sci. **47**, 7447 (2012).